

High Order Particle Transport for PIC Simulations of Plasma Flows

A thesis accepted by the Faculty of Aerospace Engineering and Geodesy of the
Universität Stuttgart in partial fulfilment of the requirements for the degree of
Doctor of Engineering Sciences (Dr.-Ing.)

by

Martin Quandt

born in Berlin

main referee : Prof. Dr. Claus-Dieter Munz
co-referee : Prof. Dr. Sabine Roller
Date of defence : 22.09.2010

Institut of Aerodynamics and Gasdynamics
Universität Stuttgart
2010

Für Meta, Magret, Willi Karl-Otto, Werner,
Ingeborg und Klaus-Werner.

Preface

This thesis was developed during my work as scientific employee at the Institut für Aerodynamik und Gasdynamik (IAG) of the Universität Stuttgart.

Many thanks to my doctoral supervisor Prof. Dr. Claus-Dieter Munz for the exceptional working conditions in his research group, especially for all the scientific freedom I was granted under his supervision. My best thanks to Dr. Rudolf Schneider from the Forschungszentrum Karlsruhe for his patient support in the field of plasma physics and his valuable linguistic suggestions.

The work was financed by the Landesstiftung Baden-Württemberg from October 2004 to November 2006 and I also wish to thank Prof. Dr. Claus-Dieter Munz and the Institut für Aerodynamik und Gasdynamik for financial support in the years up to 2009.

Many thanks also to all my colleagues at IAG for the good working atmosphere and all the fruitful scientific discussions they had with me in the last three years.

Stuttgart, January 22nd 2010

Martin Quandt

Contents

Symbols	9
Abbreviations	11
Kurzfassung	13
Abstract	15
1 Introduction	17
1.1 Motivation and Scientific Context	17
1.2 Objectives of this Work	19
1.3 Outline	19
2 Non Equilibrium Charged Particle Flows	21
2.1 Boltzmann Equation for Rarefied Plasma Flows	21
2.1.1 Source Terms of the Boltzmann Equations	22
2.1.2 The Maxwell-Vlasov Equation	22
2.1.3 The Maxwell-Lorentz Equation	24
2.2 A Numerical Model for Computational Plasma Physics	25
2.2.1 Exchange of Mesh and Particle Based Information	26
2.2.2 Finite Volume Solver for the PIC Cycle	29
3 Particle Push Methods	33
3.1 The leapfrog scheme of Boris	33
3.2 Runge-Kutta Method	37
3.3 Taylor Series Expansion	41
3.3.1 High Order Derivatives of the Inverse Lorentz Factor	44
3.3.2 High Order Derivatives of the Relativistic Velocity	45
3.4 General Aspects of Implementation	47

4	Approximation Characteristics and Validation of the Taylor Series Expansion Method	51
4.1	Non-relativistic Charged Particle Motion	52
4.1.1	Set up of the Numerical Experiment and Results	53
4.2	Particle Motion in a Space and Time Dependent E-Field	59
4.2.1	Set up of the Numerical Experiment and Results	61
4.3	Relativistic Particle Motion in a B-Field	71
4.3.1	Set up of the Numerical Experiment and Results	72
4.4	Relativistic $E \times B$ Drift	77
4.4.1	Set up of the Numerical Experiment and Results	78
4.5	Assessment of the Numerical Results	83
5	Conclusion and Outlook	87
	Bibliography	89
A	Details on Particle Push Methods	93
A.1	General Order of Calculation Steps for Taylor Series Expansion . .	93
A.2	TE Method first Order Terms	94
A.3	TE Method second Order Terms	95
A.4	TE Method third Order Terms	96
A.5	Coefficients of Runge-Kutta Integration Schemes	97
B	Some Results of Special Theory of Relativity	101
B.1	Transformation of Tensors of Rank one (4-vectors)	101
B.1.1	Basic 4-vectors	102
B.2	Transformation of electromagnetic Fields	102
B.2.1	Solution of the Energy-Moment Equation in K'	102
C	Some Properties of the Maxwell Equations	105
D	Exact Riemann solver for Maxwell System of Equations	107
D.1	General Aspects	107
D.2	Calculation of the Physical Flux	110

Symbols

\underline{b}	unit vector of magnetic induction
\underline{B}	magnetic induction
$\underline{\mathcal{B}}$	magnetic field multiplied with charge to mass ratio
c	speed of light
$\mathcal{D}^{(\kappa)}$	κ th total derivative operator
eN	Euclidian error norm
\underline{E}	electric field
$\underline{\mathcal{E}}$	electric field multiplied with charge to mass ratio
f_α	velocity distribution function of plasma species α
\underline{F}_L	Lorentz force
$\underline{\mathcal{F}}$	electromagnetic fields
\underline{j}	vector of current density
$\underline{\mathcal{K}}$	selected formal order
m	mass of particle
m_0	rest mass of particle
$M_{\alpha;\nu}$	mass of ν -th macro particle of species α
\underline{p}	relativistic impulse
q	charge of particle
q_{num}	numeric computed value
q_{ana}	analytic computed value
\underline{q}	vector of charge and current density
$\underline{Q}_{\alpha;\nu}$	charge of ν -th macro particle of species α
\underline{U}	relativistic velocity
\underline{v}	velocity of particle
\underline{v}_D	drift velocity
\underline{x}	position of particle

Symbols

α	plasma species
α_κ	Runge-Kutta coefficient at intermediate stage κ
$\beta_{\kappa\lambda}$	Runge-Kutta coefficient at $\kappa\lambda$
γ	Lorentz factor
γ_κ	Runge-Kutta coefficient at intermediate stage κ
γ_D	relativistic factor calculated with drift velocity \underline{v}_D
$\hat{\gamma}$	inverse Lorentz factor
δ	discretization time interval
ϵ_0	electric permittivity
μ_0	magnetic permeability
ρ	charge density
ω	angular velocity

Abbreviations

rhs	right hand side
EOC	effective order of convergence
FP	Fokker-Planck
FV	finite volume
MHD	magnetohydro dynamics
MV	Maxwell-Vlasov
PIC	particle in cell
LF	leapfrog
RK	Runge-Kutta
TE	Taylor series expansion



Kurzfassung

Methode höherer Ordnung zur Bewegung von Ladungsträgern für ein PIC-Verfahren in der numerischen Simulation von Plasmaströmungen

Für die numerische Simulation von Plasmaströmungen mit Hilfe der Particle in Cell (PIC) Technik wird in dieser Arbeit ein neues Verfahren zur Berechnung der relativistischen Bewegung von Ladungen in elektromagnetischen Feldern vorgestellt. Diese neue explizite Einschritt-Integrationsmethode basiert auf der Taylorreihenentwicklung der Geschwindigkeit.

Als Vergleich werden in dieser Arbeit die explizite Leapfrog-Methode nach Boris, sowie ein explizites Runge-Kutta Verfahren verwendet. Die spezielle, aber einfache Konstruktion des Leapfrog-Verfahrens nach Boris ist sehr effizient und stabil. Dieses Konstruktion beschränkt das Verfahren aber auf eine Konvergenzrate 2.-ter Ordnung. Mit einem Runge-Kutta Verfahren gibt es bereits explizite Integrationsverfahren höherer Ordnung, welche jedoch die hohe Ordnung nur durch mehrfache Auswertung der Newtonschen Bewegungsgleichung an den Stützstellen erreichen. Dazu muss der gesamten PIC-Kreislauf entsprechend häufig ausgeführt werden, was den hohen zeitlichen Rechenaufwand begründet.

Die vorgestellte Taylorreihenentwicklung, angewandt auf die relativistische Newtonsche Bewegungsgleichung, ist die erste explizite Einschritt-Methode höherer Ordnung, welche zur Lösung dieser Gleichung favorisiert und angewandt wird. Die Ausführung der Reihenentwicklung bis zur gewünschten Verfahrensordnung führt auf höhere Ableitungen der relativistischen Geschwindigkeit, sowie des inversen Lorentzfaktors. Die Abhängigkeit dieser Größen von Zeit und Raum, sowie der relativistischen Geschwindigkeit selbst, führt auf einen komplizierten Ausdruck für den Differenzialoperator. Dieser Operator kann jedoch unter Ausnutzung der hierarchischen Struktur der totalen Ableitungen, durch ein Zusammensetzen aus bereits bekannten Operatoren, zur Berechnung der niederen Ableitungen, gebildet werden. Die in dem Verfahren auftretenden totalen Ableitungen der elektromagnetischen Felder werden durch die entsprechenden Ableitungsregeln aus den partiellen Ableitungen nach der Zeit und im Raum, sowie deren gemischte Ableitungen gebildet. Alle dafür notwendigen Ableitungen müssen bereits durch Verfahren höherer Ordnung zur Lösung der Maxwellgleichung gegeben sein.

Zur Bewertung der neuen Integrationsmethode und zum Nachweis der Funktion

wird die Taylorreihenentwicklung an mehreren Beispielen getestet. Für den nicht-relativistischen Bereich kann die Methode an Beispielen mit zeit- und raumabhängigen elektrischen Feldern überprüft werden. Mit dem letzten Beispiel wird das Verhalten des Verfahrens im relativistischen Bereich untersucht, wenn der Lorentzfaktor und deren Ableitungen existieren und für die gesamte Bewegung nicht mehr zu vernachlässigen sind. In allen Tests konnte nachgewiesen werden, dass die experimentell bestimmte Verfahrensordnung mit der theoretischen Konvergenzordnung bereinstimmt. Mit jeder Erhöhung der Verfahrensordnungen, konnte die Genauigkeit gesteigert werden, sowie die Effizienz der Berechnung.

Abstract

Numerical simulations of plasma flows based on the Particle in Cell (PIC) technique need a procedure for the integration of Newtons relativistic equation of motion for charged particles. In this work a new explicit single step integration method based on a Taylor series expansion of particles velocity is presented.

Up to now the most often used particle push methods are the enhanced leapfrog scheme by J.P. Boris and the classic Runge-Kutta scheme. The special construction of the explicit Boris leapfrog scheme yields to a very efficient and robust integration, but the scheme is limited to a second order convergence rate. For a high order explicit integration the Runge-Kutta method is the only one and achieves its convergence rates by evaluating Newton's equation of motion at different interim stages. The calculation of the these stages with the complete PIC cycle is the most expensive part of this scheme. Both methods serve as a reference in this work.

The presented truncated Taylor series expansion applied on Newtons equation of motion for charged particle is the first high order explicit single step integration method. The realization of this expansion up to the desired truncation order yields to higher total derivatives of the relativistic velocity and the inverse Lorentz factor. The dependency of these derivatives in time, space and the relativistic velocity itself leads to a complex differential operator. To compute the higher total derivatives of the relativistic velocity, the hierarchical structure of this procedure is utilized to construct the operators by a rearrangement of previously defined operators. Furthermore the unknown total derivatives of the electromagnetic fields are replaced by the application of simple differentiation rules by the given high order partial derivatives in time and space as well as the mixed derivatives. These higher temporal and spatial derivatives of the electromagnetic fields are a prerequisite of the new integration scheme and have to be calculated by a high order Maxwell solver.

To assess and verify this new integration method the Taylor series expansion was tested on different examples in the non-relativistic case on space and time dependent electromagnetic fields and in the relativistic region where the Lorentz factor with all total derivatives are present. For all examples the experimental order corresponds to the selected formal order and a gain in accuracy and efficiency by an increase of the selected formal order is successfully demonstrated.

1 Introduction

This work is part of the project “Numerical Modeling and Simulation of Highly Rarefied Plasma Flows” a cooperation between IAG (Institute of Aerodynamics and Gas Dynamics, University Stuttgart) , IHM (Institute of Pulsed Power and Microwave Technology, Research Center Karlsruhe) , IRS (Institute of Space Systems, University Stuttgart) and HLRS (High Performance Computing Center Stuttgart) within the lunar mission program of the IRS. In the frame of this program a “small satellite” is under development where the thrust for the transfer from the earth orbit to the moon is generated by electric propulsion systems only. Of special interest for numerical simulation is the type of **P**ulsed **P**lasma **T**hruster (PPT) which is characterized by its simple construction and an operation mode of plasma pulses. The short duration of a single pulse of the order of microseconds and the degree of rarefaction, provide a plasma regime of non equilibrium condition. This work lines in a series of recent developments of a plasma code based on the **P**article **I**n **C**ell (PIC) technique for a consistent high order solution of the complete Boltzmann equation, called PicLas.

1.1 Motivation and Scientific Context

The modular design of the PicLas code offers the opportunity of being flexible during the development of new models for specific aspects in the field of plasma physics and to evaluate new algorithms for selective parts of the code. The PicLas code consists of three main building blocks as depicted in the block diagram in Figure 1.1. The second block computes momentum and energy exchanges due to particle collisions, without consideration of the Lorentz force, as well as chemical reactions by means of a **D**irect **S**imulation **M**onte **C**arlo (DSMC) based method. In the third block the Fokker-Planck module is used to model the effect of collision relaxations of electrons and ions on their velocity field.

Four modules in the first block form a PIC cycle to compute the interactions between charged particles and electromagnetic fields. To reduce the computational cost and to increase the accuracy at the same time a chance is open up with the strategy of single step high order schemes. For the construction of a con-

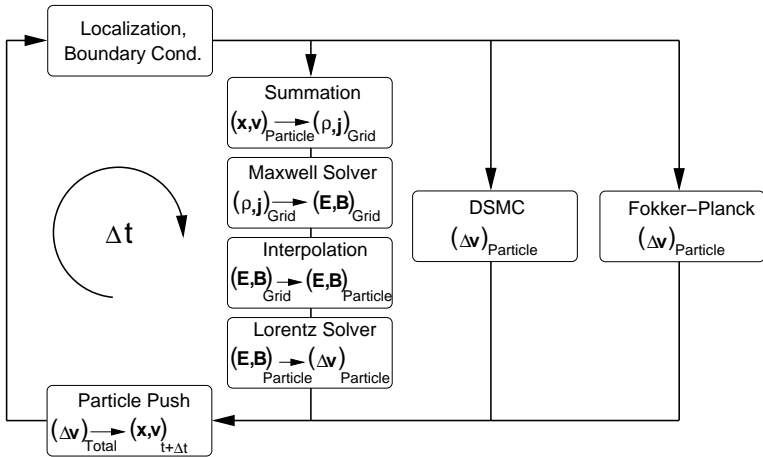


Figure 1.1: Different building blocks of the used plasma code, called PicLas.

sistent high order Maxwell-Vlasov block it is necessary that all modules inside provide the same formal order. Advances in solving hyperbolic equation systems like the Maxwell equations with high order of accuracy by applying the Cauchy-Kovalevskaya procedure founded the need for a particle treatment which sustain the order of the Maxwell solver.

Within particle treatment several implicit and explicit schemes are developed in the past [16, 3] for the integration of the relativistic equation of motion. The most commonly used methods are the Boris leapfrog method [4] proposed in 1970 and the classical Runge-Kutta integration. Both methods serve in this work as a reference. The Boris leapfrog method is an explicit scheme and separates the integration of Newtons equation of motion into an electric and magnetic part. By construction this scheme is limited to a second order convergence rate. To increase the accuracy of a simulation with the Boris scheme the discretization in time and space has to be refined. Only with the Runge-Kutta method the option of increasing the efficiency of a simulation by using a high order integration method was given. The Runge-Kutta method calculates the more accurate results with the aid of several interim stages within the given integration interval. For all interims stages the corresponding values of the electromagnetic field are needed

and have to be calculated by the complete PIC cycle. In the years of 1968 to 1972 E. Fehlberg [10, 11, 12] proposed coefficients for Runge-Kutta integration which are used in this work.

1.2 Objectives of this Work

In this work a new integration scheme of the relativistic Newton equation is presented and compared to the classical Boris leapfrog scheme and high order Runge-Kutta integration methods. The presented new integration scheme is a high order single step method and is capable to take advantage of the given higher temporal and spatial derivatives of the electromagnetic field calculated naturally by a high order Maxwell solver. To perform this Taylor series expansion, the unknown higher total derivatives of the relativistic velocity are replaced by their lower derivatives until the first derivative can be evaluated by Newtons equation of motion in the manner of a Cauchy-Kovalevskaya procedure. During this procedure additional higher total derivatives of the electromagnetic fields occur which are computed by applying differentiation rules with the given partial derivatives in time and space. These partial derivatives are a prerequisite of the new integration scheme.

1.3 Outline

In the following this work is structured into 4 chapters. In chapter 2 of this work the general microscopic model based on the Boltzmann equation is described. To compute numerically a solution of plasma flows with the strategy of the PIC approach the essential components and their interactions are explained. The part of particle computation in the PIC cycle is characterized in detail in chapter 3. The working principle of the Boris leapfrog scheme and the Runge-Kutta method for the integration of Newton's equation of motion for charged particles is given and followed by the presentation of the Taylor series expansion in detail. Chapter 4 presents four numeric experiments to validate and asses the schemes based on the Taylor series expansion approach. The accuracy and efficiency of the new integration method is compared to the classic Boris leapfrog scheme and the Runge-Kutta process.

2 Non Equilibrium Charged Particle Flows

To model the physics of a fluid consisting of charged particles from a macroscopic point of view a continuous approach, as a two fluid model is appropriate. Here the fundamental laws of conservation of mass, momentum and energy are linked with the relations of electrodynamics and Ohm's resistive law. Further approximations finally result in the equations of magneto hydro dynamics [22].

The plasma flows of interest in this thesis are characterized by very low densities and in parts of high energy particles, where relativistic effects occurs. As a consequence the continuous and close-to-equilibrium assumptions operate in their limit range and correction techniques are also hardly applicable. In these situations a kinetic description is necessary.

If we consider only a restricted physical domain and limit in particular the number of particles and the simulation time a microscopic description is numerically feasible. A further advantage of the transition to a microscopic point of view is the inclusion of physical and chemical non equilibrium states into the numerical model.

2.1 Boltzmann Equation for Rarefied Plasma Flows

To characterize the physical properties of plasma flows from the microscopic point of view the most general description is the Boltzmann equation for the velocity distribution function f_α of plasma of a species α . The function f_α defines a probability to find a particle of species α in the phase space volume $(d\underline{x}, d\underline{v})$. The evolution of this probability function is given by (see, for instance [26, 18])

$$\frac{\partial f_\alpha}{\partial t} + \underline{v} \cdot \nabla_x f_\alpha + \underline{a} \cdot \nabla_v f_\alpha = \left(\frac{\delta f_\alpha}{\delta t} \right)_{col} . \quad (2.1)$$

The total derivative of f_α on the left side consists of the temporal derivative, the propagation of f_α in the spatial domain with velocity \underline{v} and in velocity space with acceleration \underline{a} . The dynamic evolution of this function is affected by the source term on the right hand side rhs, which takes the collisional contributions of the particles into account.

2.1.1 Source Terms of the Boltzmann Equations

The sources on the rhs of (2.1) is the Boltzmann collision integral and represents the rate of change of f_α due to microscopic particle collisions. It can be written as

$$\left(\frac{\delta f_\alpha}{\delta t}\right)_{col} = \sum_\beta n_\beta(\underline{x}, t) \int d^3w d\Omega g Q_{\alpha\beta} \left[f_\alpha(\underline{v}') f_\beta(\underline{w}') - f_\alpha(\underline{v}) f_\beta(\underline{w}) \right], \quad (2.2)$$

where the prime refers to the value of a quantity after a collision ($\underline{v}' = \underline{v} + \Delta\underline{v}$ and $\underline{w}' = \underline{w} + \Delta\underline{w}$) and unprimed denotes the values before the collision. The index β runs over all “scattering” populations (also called field particles), $\underline{g} = \underline{v} - \underline{w}$ is the relative velocity, $Q_{\alpha\beta} = Q_{\alpha\beta}(g, \theta, \phi)$ is the differential scattering cross section between the particles of the species α and β . The element of solid angle $d\Omega$ is given by $d\Omega = \sin\theta d\theta d\phi$, where θ and ϕ denote the scattering and azimuthal angle, respectively. In the situation of charged particle collisions the differential cross section is given by the classical Rutherford formula. Then, for small changes in velocity the collision integral can be approximated. After some straightforward manipulations and reformulations one obtains the Fokker-Planck (FP) equation (see, for instance, [24, 19])

$$\left(\frac{\delta f_\alpha}{\delta t}\right)_{col} = \sum_\beta \left\{ - \sum_j \frac{\partial}{\partial v_j} \left(F_j^{(\alpha\beta)} f_\alpha \right) + \frac{1}{2} \sum_{j,k} \frac{\partial^2}{\partial v_k^2} \left(D_{jk}^{(\alpha\beta)} f_\alpha \right) \right\}, \quad (2.3)$$

which represents the lowest order approximations of the Boltzmann integral. The central quantities in the latter equation are the coefficients of the dynamical friction force $F_j^{(\alpha\beta)} = F_j^{(\alpha\beta)}(\underline{v}, \underline{x}, t)$ and the diffusion tensor $D_{jk}^{(\alpha\beta)} = D_{jk}^{(\alpha\beta)}(\underline{v}, \underline{x}, t)$. The indices j and k runs over all three space dimensions and denote the components of corresponding quantities. Very recently the FP collision operator (2.3) for elastic electron-electron and electron-ion Coulomb scattering in a plasma has been solved numerically on the basis of PIC methods [7].

2.1.2 The Maxwell-Vlasov Equation

A class of plasma flows characterized by dominating collective effects when individual events of particle interactions become less significant, the collision term in (2.1) can be neglected, and one obtains the Vlasov equation (see, e.g. [20] and references given therein) where the total derivative d/dt of function f_α vanishes.

In this case function f_α is conserved and (2.1) is a transport equation of function f_α

$$\frac{\partial f_\alpha}{\partial t} + \underline{v} \cdot \nabla_x f_\alpha + \frac{\underline{F}_L}{m_\alpha} \cdot \nabla_p f_\alpha = 0, \quad \underline{x} \in \mathbb{D} \subset \mathbb{R}^3, \quad \underline{p} \in \mathbb{R}^3, \quad t > 0. \quad (2.4)$$

Here, $(\underline{x}, \underline{p})$ is a point in phase space $\mathbb{D} \times \mathbb{R}^3$, ∇_p denotes the derivative with respect to the relativistic momentum

$$\underline{p} = m_\alpha \gamma \underline{v} \quad (2.5)$$

where the relativistic Lorentz factor γ is defined as $\gamma^2 = 1 + \left(\frac{\underline{p}}{m_\alpha c}\right)^2$ with the speed of light in vacuum c (see Appendix B for more details). The Lorentz force \underline{F}_L is given by

$$\underline{F}_L(\underline{v}, \underline{x}, t) = q_\alpha \left[\underline{E}(\underline{x}, t) + \underline{v} \times \underline{B}(\underline{x}, t) \right]. \quad (2.6)$$

The evolution of the electromagnetic fields which appear in the Lorentz force is given by the full set of Maxwell equations in vacuum. This system consists of the two hyperbolic evolution equations

$$\frac{\partial \underline{E}}{\partial t} - c^2 \nabla_x \times \underline{B} = -\epsilon_0^{-1} \underline{j}, \quad (2.7)$$

$$\frac{\partial \underline{B}}{\partial t} + \nabla_x \times \underline{E} = 0, \quad (2.8)$$

and the elliptic part established by Gauss law and the divergence-free condition for the magnetic induction

$$\nabla_x \cdot \underline{E} = \epsilon_0^{-1} \rho, \quad (2.9)$$

$$\nabla_x \cdot \underline{B} = 0, \quad (2.10)$$

where ρ and \underline{j} denote the charge and current density, respectively. To extend Maxwells equation system to the evolution of the electromagnetic fields in materials, a substitution is needed of the electric and magnetic field in equation (2.7) and the divergence condition (2.9) by $\underline{D} = \epsilon \underline{E}$ and $\underline{B} = \mu \underline{H}$. Here μ and ϵ denote the electric permittivity and the magnetic permeability of the material. With the values in vacuum μ_0 and ϵ_0 the speed of light in vacuum is define by $\epsilon_0 \mu_0 c^2 = 1$. The self consistent interplay of the particle distribution function with the electromagnetic fields is manifested by calculating the lowest moments of all distribution

functions:

$$\rho(\underline{x}, t) = \sum_{\sigma} q_{\sigma} \int_{\mathbb{R}^3} d^3 p f_{\sigma}(\underline{p}, \underline{x}, t), \quad (2.11)$$

$$\underline{j}(\underline{x}, t) = \sum_{\sigma} q_{\sigma} \int_{\mathbb{R}^3} d^3 p \underline{v}(\underline{p}) f_{\sigma}(\underline{p}, \underline{x}, t), \quad (2.12)$$

where the sums run over all species in the plasma. These source terms for the Maxwell equations (2.7),(2.9) together with the conservation equation (2.4) for the distribution function f_{α} set up the time dependent non linear Maxwell-Vlasov (MV) problem.

2.1.3 The Maxwell-Lorentz Equation

A highly effective and powerful strategy to tackle the MV equations numerically is based on particle methods [16, 3]. Here, the (continuous) solution f_{α} of the Vlasov equation (2.4) is approximated by a set of N_{α} discrete fluid elements, usually called macroparticles. The macroparticles are centered at the phase space coordinates $(\underline{x}_{\nu}(t), \underline{p}_{\nu}(t))_{1 \leq \nu \leq N_{\alpha}}$ and possess (constant) weights ω_{ν} which may be interpreted as the number of elementary constituents of the ν^{th} particle. This particle approximation \tilde{f}_{α} consists of a linear combination of Dirac functions in phase space and reads as

$$\tilde{f}_{\alpha}(\underline{p}, \underline{x}, t) = \sum_{\nu=1}^{N_{\alpha}} \omega_{\nu} \delta[\underline{p} - \underline{p}_{\nu}(t)] \delta[\underline{x} - \underline{x}_{\nu}(t)]. \quad (2.13)$$

Note, that this discrete distribution function also satisfies the Vlasov equation (2.4) (in the sense of distributions; see, e.g. [21]). For this, one applies the theory of characteristics to the Vlasov equation and obtains that the macroparticles are transported according to the classical laws of dynamics

$$\frac{d}{dt} [\gamma_{\nu}(t) \underline{v}_{\nu}(t)] = \frac{Q_{\alpha; \nu}}{M_{\alpha; \nu}} \left[\underline{E}(\underline{x}_{\nu}(t), t) + \underline{v}_{\nu} \times \underline{B}(\underline{x}_{\nu}(t), t) \right], \quad (2.14)$$

$$\frac{d\underline{x}_{\nu}(t)}{dt} = \underline{v}_{\nu}(t) \quad (2.15)$$

with given initial data $\underline{x}_{\nu}(0)$ and $\underline{v}_{\nu}(0)$ along the characteristics, where $\gamma_{\nu}(t)$ denotes the relativistic factor. These equations – also called Lorentz equations –

describe the evolution of the ν -th macroparticle with mass $M_{\alpha;\nu} = \omega_\nu m_\alpha$ and charge $Q_{\alpha;\nu} = \omega_\nu q_\alpha$ in phase space due to the external and/or self fields \underline{E} and \underline{B} . It is noteworthy to mention that the number of elementary constituents cancels out in equation (2.14) and the motion of a macroparticle is the same as a single charge of species “ α ”. Finally, using the discrete distribution function (2.13) to perform the integrations in (2.11) and (2.12), the source terms of the Maxwell equations now read as

$$\rho(\underline{x}, t) = \sum_{\sigma} \sum_{\nu=1}^{N_{\sigma}} Q_{\sigma;\nu} \delta[\underline{x} - \underline{x}_{\nu}(t)] \quad (2.16)$$

$$\underline{j}(\underline{x}, t) = \sum_{\sigma} \sum_{\nu=1}^{N_{\sigma}} Q_{\sigma;\nu} \underline{v}_{\nu}(\underline{p}_{\nu}) \delta[\underline{x} - \underline{x}_{\nu}(t)]. \quad (2.17)$$

The Maxwell equations with these source terms and the Lorentz equations form together the Maxwell-Lorentz model, the starting point of numerical approximations.

2.2 A Numerical Model for Computational Plasma Physics

Studying kinetic effects, in particular, in plasma physics a sufficiently large amount of macroparticles is necessary. However, the calculation of all direct particle-particle Coulomb forces is hardly possible even on nowadays supercomputers. Especially for very large systems, a tractable way to circumvent this difficulty is the PIC method [16, 3] which has a history over more than five decades [2].

The peculiarities of the PIC method are the powerful particle-mesh techniques (see Fig. 2.1) that couple an Eulerian grid based model for the solution of Maxwell equation with a Lagrangian particle based solver for the laws of dynamics (2.14) and (2.15). To explain a PIC cycle run for one timestep of Δt (see Fig. (2.1)) the starting point is set to module **Assignment**. This module transfers particle based data of charge and current density from Lagrangian into the Eulerian space. At first a localization for each particle is necessary to get the cell that contains it, then the charge and current density may also be assigned to surrounding nodes or cells according to the chosen shape function.

With the sources at the current time level the evolution of the electromagnetic fields up to time level $t + \Delta t$ is obtained by the numerical solution of the Maxwell equations in the module **Maxwell Solver**.

With module **Interpolation** the electromagnetic fields calculated in the Eulerian space are transferred to the Lagrangian space by interpolating the fields onto par-

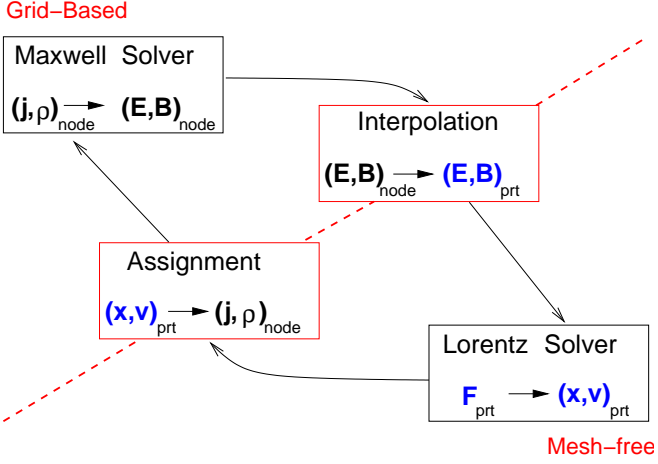


Figure 2.1: Different building blocks of the classical PIC-approach.

tile positions. When the electromagnetic force on particle positions is known, the new phase space coordinates are determined by solving numerically the Lorentz equations in module Lorentz Solver.

2.2.1 Exchange of Mesh and Particle Based Information

In order to obtain $\rho(\underline{x}, t)$ and $\underline{j}(\underline{x}, t)$ everywhere in the space, at the nodes or center of cells of the computational grid (where the Maxwell equations are solved) some kind of regularization is necessary. The regularization is established by a convolution of the charge and current density with the (shape) function S according to

$$\rho_h(\underline{x}, t) = \int_{-\infty}^{\infty} d^3u S(\underline{x} - \underline{u}) \rho(\underline{u}, t) = \sum_{\sigma} \sum_{\nu=1}^{N_{\sigma}} Q_{\sigma; \nu} S(\underline{x} - \underline{x}_{\nu}(t)) \quad (2.18)$$

and

$$\underline{j}_h(\underline{x}, t) = \int_{-\infty}^{\infty} d^3u S(\underline{x} - \underline{u}) \underline{j}(\underline{u}, t) = \sum_{\sigma} \sum_{\nu=1}^{N_{\sigma}} Q_{\sigma; \nu} \underline{v}_{\nu} S(\underline{x} - \underline{x}_{\nu}(t)), \quad (2.19)$$

respectively, where the subscript indicates the assignment to a grid cell h . It is common to use for the shape function B-splines of fixed order [16]. In the following we introduce discrete B-splines which are interesting for numerical purposes. For this we start with the right side normalized rectangular “top hat” function defined as

$$\beta_{[i,i+1]}^{[0]}(x) = \beta_{[x_i,x_{i+1}]}^{[0]}(x) = \begin{cases} 1, & \text{if } x \in [x_i, x_{i+1}) \\ 0, & \text{otherwise} \end{cases}. \quad (2.20)$$

Then, the higher-order discrete B-splines are constructed recursively according to

$$\begin{aligned} \beta_{[i,\dots,i+k+1]}^{[k]}(x) &= \frac{x - x_i}{x_{i+k} - x_i} \beta_{[i,\dots,i+k]}^{[k-1]}(x) \\ &+ \frac{x_{i+k+1} - x}{x_{i+k+1} - x_{i+1}} \beta_{[i+1,\dots,i+k+1]}^{[k-1]}(x). \end{aligned} \quad (2.21)$$

It can be shown by induction [23] that these splines have the following properties

$$\beta_{[i,\dots,i+k+1]}^{[k]}(x) = 0, \quad x \notin (x_i, x_{i+1}), \quad k \geq 1, \quad (2.22)$$

$$\beta_{[i,\dots,i+k+1]}^{[k]}(x) \in (0, 1], \quad x \in (x_i, x_{i+1}), \quad (2.23)$$

$$\sum_{i=-\infty}^{\infty} \beta_{[i,\dots,i+k+1]}^{[k]}(x) = \sum_{i=j-k}^k \beta_{[i,\dots,i+k+1]}^{[k]}(x) = 1, \quad \forall x \in [x_j, x_{j+1}]. \quad (2.24)$$

Applying the recursion relation (2.21) with (2.20), one explicitly obtains for the discrete B-splines up to third order

$$\beta_{[i,i+1,i+2]}^{[1]}(x) = \frac{x - x_i}{H} \beta_{[i,i+1]}^{[0]}(x) + \frac{x_{i+2} - x}{H} \beta_{[i+1,i+2]}^{[0]}(x), \quad (2.25)$$

$$\begin{aligned} \beta_{[i,i+1,i+2,i+3]}^{[2]}(x) &= \frac{(x - x_i)^2}{2H^2} \beta_{[i,i+1]}^{[0]}(x) \\ &+ \left[\frac{(x - x_{i+1})(x_{i+2} - x)}{H^2} + \frac{1}{2} \right] \beta_{[i+1,i+2]}^{[0]}(x) \\ &+ \frac{(x_{i+3} - x)^2}{2H^2} \beta_{[i+2,i+3]}^{[0]}(x) \end{aligned} \quad (2.26)$$

and

$$\begin{aligned}
 & \beta_{[i,i+1,i+2,i+3,i+4]}^{[3]}(x) \\
 &= \frac{(x-x_i)^3}{6H^3} \beta_{[i,i+1]}^{[0]}(x) \\
 &+ \left[\frac{(x-x_{i+1})^2(x_{i+2}-x)}{2H^3} + \frac{(x-x_{i+1})}{2H} + \frac{1}{6} \right] \beta_{[i+1,i+2]}^{[0]}(x) \\
 &+ \left[\frac{(x-x_{i+2})(x_{i+3}-x)^2}{2H^3} + \frac{(x_{i+3}-x)}{2H} + \frac{1}{6} \right] \beta_{[i+2,i+3]}^{[0]}(x) \\
 &+ \frac{(x_{i+4}-x)^3}{6H^3} \beta_{[i+3,i+4]}^{[0]}(x), \tag{2.27}
 \end{aligned}$$

respectively, where equidistant grid spacing, $H = x_{i+1} - x_i$, $\forall i$, is assumed. If the ν -th particle is located at time t in the interval $x_\nu(t) \in [x_j, x_{j+1}]$, we obtain from the partition of unity property (2.24) for the B-spline of order one that

$$\beta_{[j-1,j,j+1]}^{[1]}(x_\nu) + \beta_{[j,j+1,j+2]}^{[1]}(x_\nu) = 1 \tag{2.28}$$

holds, where the first and second spline is centered around x_j and x_{j+1} (“triangle” function), respectively. As a consequence of the basic B-spline (2.20), one concludes that the assignment weights to these nodes are given by

$$W_j = \frac{x_{j+1} - x_\nu}{H} \quad \text{and} \quad W_{j+1} = \frac{x_\nu - x_j}{H}, \tag{2.29}$$

resulting in, for instance, a charge density assignment of $\rho_{j+1} = (W_j Q_{\sigma;\nu})/H$ and $\rho_j = (W_{j+1} Q_{\sigma;\nu})/H$. Vice versa, when the numerical solution of the Maxwell equations is available in the nodes of the computational grid, then, for example, the electrical field at the particle position $x_\nu(t)$ is given by

$$\begin{aligned}
 \underline{E}(x_\nu, t) &= \beta_{[j-1,j,j+1]}^{[1]}(x_\nu) \underline{E}_j + \beta_{[j,j+1,j+2]}^{[1]}(x_\nu) \underline{E}_{j+1} \\
 &= W_j \underline{E}_j + W_{j+1} \underline{E}_{j+1}, \tag{2.30}
 \end{aligned}$$

which represents a linear interpolation of the field onto the particle location. Note however, that in the case of B-spline kernels greater than one, the determination of the electromagnetic fields at the particle position is no longer an interpolation, because the fields enter with additional, not position dependent weightings. For

instance, a B-spline of order three yields

$$\begin{aligned}
 \underline{E}(x_\nu, t) &= \frac{(x_{j+1} - x_\nu)^3}{6 H^3} \underline{E}_{j-1} \\
 &+ \left[\frac{(x_\nu - x_j)(x_{j+1} - x_\nu)^2}{2 H^3} + \frac{(x_{j+1} - x_\nu)}{2 H} + \frac{1}{6} \right] \underline{E}_j \\
 &+ \left[\frac{(x_\nu - x_j)^2(x_{j+1} - x_\nu)}{2 H^3} + \frac{(x_\nu - x_j)}{2 H} + \frac{1}{6} \right] \underline{E}_{j+1} \\
 &+ \frac{(x_\nu - x_j)^3}{6 H^3} \underline{E}_{j+2}.
 \end{aligned} \tag{2.31}$$

Finally, we remark that the B-spline approach can be extended in straightforward manner when a structured computational grid is available. For example, in two spatial dimensions the first order B-spline kernel provide the well-known area-weighting method for squares and rectangles which can be further augmented to the linear volume weighting technique [8].

2.2.2 Finite Volume Solver for the PIC Cycle

In order to sketch out briefly the finite volume (FV) approach for the Maxwell equations, it is convenient to use the conservation form of the Maxwell equations which is the system of linear hyperbolic evolution equations

$$\frac{\partial \underline{u}}{\partial t} + \sum_{i=1}^3 \underline{K}_i \frac{\partial \underline{u}}{\partial x_i} = \underline{s}, \tag{2.32}$$

where

$$\underline{u}(\underline{x}, t) = (E_x, E_y, E_z, B_x, B_y, B_z)^T \tag{2.33}$$

and $\partial/\partial x_i$ abbreviates the derivation with respect to space. The block structured matrices $\underline{K}_i \in \mathbb{R}^{6 \times 6}$ are given by

$$\underline{K}_i = \begin{pmatrix} \underline{0} & c^2 \underline{M}_i \\ \underline{M}_i^T & \underline{0} \end{pmatrix} \quad i = 1, 2, 3 \tag{2.34}$$

with the 3×3 matrices

$$\underline{M}_1 = \begin{pmatrix} 0 & 0 & 0 \\ 0 & 0 & 1 \\ 0 & -1 & 0 \end{pmatrix}, \quad \underline{M}_2 = \begin{pmatrix} 0 & 0 & -1 \\ 0 & 0 & 0 \\ 1 & 0 & 0 \end{pmatrix}, \tag{2.35}$$

$$\underline{\underline{M}}_3 = \begin{pmatrix} 0 & 1 & 0 \\ -1 & 0 & 0 \\ 0 & 0 & 0 \end{pmatrix}. \quad (2.36)$$

For more details concerning the Maxwell equations in conservation form we refer the reader to Appendix C. The source term on the right hand side of equation (2.32) reads as

$$\underline{s}(\underline{x}, t) = -\epsilon_0^{-1} (j_x, j_y, j_z, 0, 0, 0)^T, \quad (2.37)$$

where the components of the current density enters only.

We assume that the domain of computation Q is discretized by N non-overlapping grid cells C_i – that is $Q = \bigcup_{i=1}^N C_i$ – each with $F_{i,\alpha}$, $\alpha = 1, \dots, \sigma_i$, faces and volume V_i . Then, the integration of the conservation equation (2.32) over the space time volume $C_i \times [t_0, t]$, $t > t_0$, yields the evolution equation

$$\begin{aligned} V_i [\underline{u}_i(t) - \underline{u}_i(t_0)] &+ \sum_{\alpha=1}^{\sigma_i} \int_{t_0}^t \int_{F_{i,\alpha}} \left[\sum_{j=1}^3 n_j^{(i,\alpha)} \underline{\underline{K}}_j \underline{u}(\underline{x}, t) \right] dF dt \\ &= \int_{t_0}^t \int_{V_i} \underline{s}(\underline{x}, t) dV dt \end{aligned} \quad (2.38)$$

for the cell averaged state variable

$$\underline{u}_i(t) = \frac{1}{V_i} \int_{V_i} \underline{u}(\underline{x}, t) dV, \quad (2.39)$$

where Gauss law is already used to “shift” the divergence and $n_j^{(i,\alpha)}$ are the components of the outwards directed unit normal at face $F_{i,\alpha}$. To obtain the numerical solution $\underline{u}_i(t^{n+1})$ at $t = t^{n+1}$ from the given one $\underline{u}_i(t^n)$ at $t = t^n$ we apply the second order accurate Strang splitting in time in the following form.

First, we consider the influence of the source over a half time step according to

$$\underline{u}_i^{*1}(t^{n+1/2}) = \underline{u}_i^{*1}(t^n) + \int_{t^n}^{t^{n+1/2}} \int_{V_i} \underline{s}(\underline{x}, t) dV dt \quad (2.40)$$

with initial values $\underline{u}_i^{*1}(t^n) = \underline{u}_i(t^n)$. Afterwards, the solution of the homogeneous evolution equation over the full interval $[t^n, t^{n+1}]$ is computed from

$$\underline{u}_i^{*2}(t^{n+1}) = \underline{u}_i^{*2}(t^n) - \frac{1}{V_i} \sum_{\alpha=1}^{\sigma_i} \int_{t^n}^{t^{n+1}} \int_{F_{i,\alpha}} \left[\sum_{j=1}^3 n_j^{(i,\alpha)} \underline{K}_j \underline{u}_i^{*2}(\underline{x}, t) \right] dF dt, \quad (2.41)$$

where the initial data are now given by $\underline{u}_i^{*2}(t^n) = \underline{u}_i^{*1}(t^{n+1/2})$. In the final step, once again the influence of the source term is taken into account for another half time step. With the initial values $\underline{u}_i^{*3}(t^n) = \underline{u}_i^{*2}(t^{n+1})$ one obtains

$$\underline{u}_i^{*3}(t^{n+1}) = \underline{u}_i^{*3}(t^n) + \int_{t^n}^{t^{n+1/2}} \int_{V_i} \underline{s}(\underline{x}, t) dV dt, \quad (2.42)$$

which yields the desired solution at $t = t^{n+1}$, namely, $\underline{u}_i^{n+1} = \underline{u}_i^{*3}(t^{n+1})$.

In the context of FV approximation one defines the numerical flux as an appropriate approximation of the time-averaged physical flux through the boundary face $F_{i,\alpha}$ and writes for the integrals occurring in (2.41)

$$\underline{G}_{i,\alpha}^{n+1/2} \approx \frac{1}{\Delta} \int_{t^n}^{t^{n+1}} \int_{F_{i,\alpha}} \underline{A}_{i,\alpha} \underline{u}_i^{*2}(\underline{x}, t) dF dt, \quad (2.43)$$

where the abbreviation

$$\underline{A}_{i,\alpha} = \sum_{j=1}^3 n_j^{(i,\alpha)} \underline{K}_j \quad (2.44)$$

is introduced (see Appendix C). With this definition the explicit FV scheme takes the compact form

$$\underline{u}_i^{*2}(t^{n+1}) = \underline{u}_i^{*2}(t^n) - \frac{\Delta t}{V_i} \sum_{\alpha=1}^{\sigma_i} \underline{G}_{i,\alpha}^{n+1/2} \quad (2.45)$$

for element C_i of the computational grid. Clearly, the numerical flux (2.43) depends on the state vector \underline{u}_i^{*2} at the common face of two elements and is only well defined for continuous and smooth variable vectors. In the case of discontinuous data at the interface of two elements, the numerical flux results from the solution of a Riemann problem as shown by Godunov [14]. The construction of a Riemann solver for the Maxwell equations from piecewise constant averaged initial data is described in Appendix D.

3 Particle Push Methods

Starting from the Lorentz force (2.6), we consider here the equations of particle motion in the form

$$\frac{d}{dt}\underline{p} = q(\underline{E} + \underline{v} \times \underline{B}), \quad (3.1)$$

$$\frac{d}{dt}\underline{x} = \underline{v}, \quad (3.2)$$

where the relativistic momentum \underline{p} is given by $\underline{p} = m_\alpha \gamma \underline{v}$. In the following we consider only one species and drop the subscript α for simplicity.

With an integration of equation (3.1) the new velocity is obtained and the second integration leads to the corresponding new position in space. The most often used explicit integrators are the Boris leapfrog (LF) approach and the Runge-Kutta (RK) method. In the context of the present work we introduce a new, explicit single step technique based on Taylor series expansion (TE). For a more clear comparison with the new TE approach the construction of the classic schemes and the interplay with the complete PIC cycle is described in detail.

3.1 The leapfrog scheme of Boris

For the sake of completeness we briefly recall here the basic features of the leapfrog scheme introduced by Boris [4], which takes into account the special structure of the Lorentz force. The discretization of the relativistic equations of motion (3.1,3.2) has been described extensively in the literature [4, 16, 3, 28, 9] and can be written with the time centered velocity \underline{v} and the relativistic velocity \underline{U} as

$$\left(\underline{U}^{n+1/2} - \alpha \underline{E}^n\right) - \left(\underline{U}^{n-1/2} + \alpha \underline{E}^n\right) = \frac{2\alpha}{\gamma^n} \underline{U}^n \times \underline{B}^n, \quad (3.3)$$

$$\underline{x}^{n+1} - \underline{x}^n = \Delta t \underline{v}^{n+1/2}, \quad (3.4)$$

where $\alpha = \frac{q\Delta t}{2m}$ and the relativistic velocity is computed from

$$\underline{U}(t) = \gamma \underline{v}(t) \quad (3.5)$$

with

$$\gamma^2 = \frac{1}{1 - \frac{|\underline{u}|^2}{c^2}} = 1 + \frac{|\underline{U}|^2}{c^2}. \quad (3.6)$$

Furthermore, Δt is the time step size and n denotes the actual time level. Note,

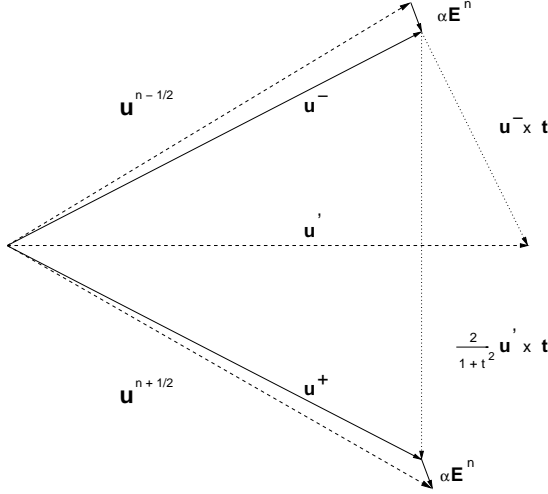


Figure 3.1: Geometrical illustration of the second order accurate Boris scheme.

that the electromagnetic fields are given at position \underline{x}^n . Obviously, the right-hand side (rhs) of (3.4) is time-centered around $t^{n+1/2} = (n+1/2)\Delta t$ while that of (3.3) has to be computed at $t^n = n\Delta t$, leading to a second order accurate integration scheme. For the following it is convenient to introduce the quantities

$$\underline{u}^- = \underline{U}^{n-1/2} + \alpha \underline{E}^n, \quad (3.7)$$

$$\underline{u}^+ = \underline{U}^{n+1/2} - \alpha \underline{E}^n, \quad (3.8)$$

where \underline{U}^n is replaced by its average value $\frac{1}{2} (\underline{U}^{n-1/2} + \underline{U}^{n+1/2})$. The relativistic Lorentz factor is approximated by $\gamma^n \approx \gamma^- = \sqrt{1 + |\underline{u}^-|^2/c^2}$ with velocity \underline{u}^- , obtained after the first “half-acceleration” described by (3.7). Then, equation (3.3)

can be recast into the form

$$\underline{u}^+ - \underline{u}^- = (\underline{u}^+ + \underline{u}^-) \times \underline{t}, \quad (3.9)$$

where the auxiliary vector \underline{t} is defined by

$$\underline{t} = \frac{\alpha}{\gamma^-} |\underline{B}^n| \underline{b}^n, \quad \underline{b}^n = \frac{\underline{B}^n}{|\underline{B}^n|}. \quad (3.10)$$

For the latter relation (3.10) it is easy to prove that $\underline{t} \cdot \underline{u}^+ = \underline{t} \cdot \underline{u}^-$ and $|\underline{u}^+| = |\underline{u}^-|$. In order to determine \underline{u}^+ from (3.10), we introduce an additional velocity vector defined by

$$\underline{u}' = \underline{u}^- + \underline{u}^- \times \underline{t}, \quad (3.11)$$

which is the sum of \underline{u}^- and the “half-rotation” of \underline{u}^- around the magnetic induction \underline{B}^n , having a length of $|\underline{u}'|^2 = (1 + |\underline{t}|^2) |\underline{u}^-|^2 - (\underline{u}^- \cdot \underline{t})^2$ (see Fig. 3.1). A further “half-rotation” but now of \underline{u}' around \underline{B}^n yields

$$\underline{u}' \times \underline{t} = \underline{u}^+ \times \underline{t} + |\underline{t}|^2 \underline{u}^+ - (\underline{u}^+ \cdot \underline{t}) \underline{t} \quad (3.12)$$

$$= \underline{u}^- \times \underline{t} - |\underline{t}|^2 \underline{u}^- + (\underline{u}^- \cdot \underline{t}) \underline{t} \quad (3.13)$$

From this relation and equation (3.9) we find that \underline{u}^+ is obtained from

$$\underline{u}^+ = \underline{u}^- + \frac{2}{1 + |\underline{t}|^2} \underline{u}' \times \underline{t}. \quad (3.14)$$

After a second “half-acceleration” by $\Delta t/2$ with the electrical field \underline{E}^n , we finally get the solution of equation (3.3), namely, the velocity at the time level $t = t^{n+1/2}$

$$\underline{U}^{n+1/2} = \underline{u}^+ + \alpha \underline{E}^n, \quad (3.15)$$

and from this result and relation (3.4) the new particle position at $t = t^{n+1}$ is computed. For the special case where \underline{t} is orthogonal to \underline{u}^- the outlined Boris LF scheme can be illustrated geometrically as it is shown in Figure (3.1).

The interplay between the Boris LF scheme and the PIC cycle is schematically depicted in Figure 3.2. At the beginning the localized position of the particles within the grid and their time shifted velocity $v^{n-\frac{1}{2}}$ are given as well as the grid based electromagnetic fields E^n, B^n from the previous iteration step or by the initialization routine, see below. In module ① the mesh based electromagnetic fields are interpolated onto particles position. With these updated values and the velocity at time $t^{n-1/2}$ the particle push module ② calculates the velocity up to

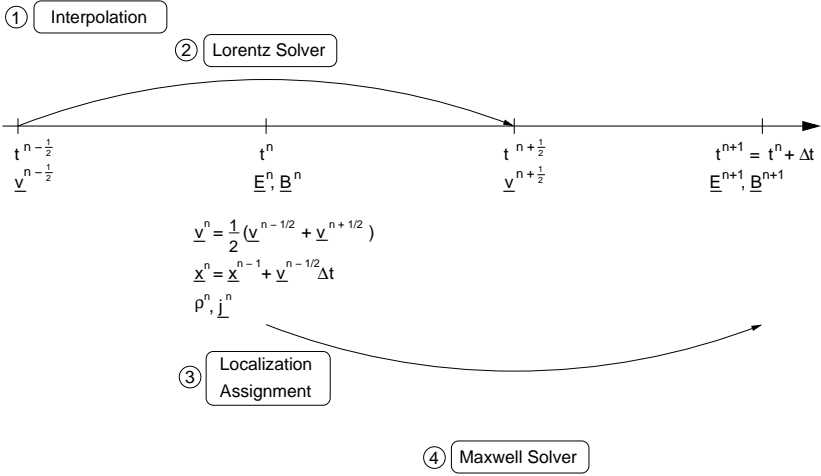


Figure 3.2: Particle push method proposed by Boris with leapfrog technique and time centered particle velocity.

$t^{n+1/2}$ and according to the isochronous leapfrog method the velocity at time t^n is computed by a linear averaging of $v^{n-1/2}$ and $v^{n+1/2}$. With an integration over Δt of velocity $v^{n-1/2}$ the position at time t^n is obtained. Based on the position and velocity the sources for each particle are calculated. In the next step the module ③ localizes the particle and assigns the contribution to the source from each particle to the corresponding nodes. With the updated values of the source terms the field solver module ④ computes the evolution of the electromagnetic fields up to time t^{n+1} . Now the cycle is closed and starts again with module ① at time t^{n+1} .

The first time step is calculated by the initialization routine to obtain the time shifted velocity field. For that reason the electromagnetic field is temporarily calculated up to time $t^{n+1/4}$ with the sources at time t^n . With these temporarily fields the leapfrog scheme in the particle push module ② calculates the velocity up to $t^{n+1/2}$. A further integration over Δt of velocity $v^{n+1/2}$ yields the position at time t^{n+1} . With the given sources at time t^n the electromagnetic fields are computed up to time t^{n+1} and the cycle of the leapfrog scheme is initialized.

3.2 Runge-Kutta Method

The classical Runge-Kutta (RK) approach is a multi-stage method that offers the possibility to integrate ordinary differential equations numerically with a convergence rate higher than two. Here, these methods are applied to the Lorentz equations (2.14) and (2.15), where in contrast to the Boris LF scheme the position and velocity are now defined at the same value of time. The common formulation of a μ -stage RK scheme for the integration of the scalar differential equation

$$\frac{dy}{dt} = e(t, y) \quad (3.16)$$

reads as

$$y = y_0 + \Delta t \sum_{\kappa=0}^{\mu} \gamma_{\kappa} e_{\kappa} , \quad (3.17)$$

where the intermediate stages are defined by

$$e_{\kappa} = e(t_{\kappa}, y_{\kappa}) \quad (3.18)$$

$$t_{\kappa} = t_0 + \alpha_{\kappa} \Delta t \quad (3.19)$$

$$y_{\kappa} = y_0 + \Delta t \sum_{\lambda=0}^{\kappa-1} \beta_{\kappa\lambda} e_{\lambda} \quad , \quad \kappa = 1, 2, 3, \dots \quad (3.20)$$

with the initial value $\kappa = 0$ with $e_0 = e(t_0, y_0)$. In the context of the present work we used for the coefficients $\alpha_{\kappa}, \beta_{\kappa\lambda}, \gamma_{\kappa}$ the values published by Fehlberg [10, 11, 12]. The peculiarity of Fehlbergs Runge-Kutta integration scheme arises from the purpose of step size control based on a complete coverage of the leading local truncation error term. To achieve this he used two equations, the first one for the solution of the differential equation with the selected formal order and the second one to estimate the truncation error of one order higher approximation. For example the two equations for a second order scheme read as

$$y = y_0 + \Delta t \sum_{\kappa=0}^2 \gamma_{\kappa} e_{\kappa} , \quad (3.21)$$

$$\hat{y} = y_0 + \Delta t \sum_{\kappa=0}^3 \hat{\gamma}_{\kappa} e_{\kappa} . \quad (3.22)$$

To solve this set of equations, where the coefficients of $\alpha_\kappa, \beta_{\kappa\lambda}$ have to be the same in both formulas, while γ_κ satisfy a second order approximation and $\hat{\gamma}_\kappa$ a third order truncation error estimation, more evaluations per steps are required than for the known classical Runge-Kutta formulas. The Taylor expansion of equation (3.21) and (3.22) up to the order of the truncation error exhibit all needed coefficients. The conditions of the Runge-Kutta coefficients, described in [5] emerging an equation system and its solution with the technique of Fehlberg leads to the coefficients of a second order scheme listed in table 3.1. The classic

κ	λ	0	1	2	γ_κ	$\hat{\gamma}_\kappa$
	α_κ	$\beta_{\kappa\lambda}$				
0	0	0			$\frac{5}{18}$	$\frac{5}{18}$
1	$\frac{1}{2}$	$\frac{1}{2}$			$\frac{1}{6}$	0
2	$\frac{3}{4}$	$\frac{3}{16}$	$\frac{9}{16}$		$\frac{5}{9}$	$\frac{8}{9}$
3	1	$\frac{5}{18}$	$\frac{1}{16}$	$\frac{5}{9}$		$-\frac{1}{6}$

Table 3.1: Coefficients of Fehlbergs second order RK integration scheme with two interims stages and three stages for an error estimation step

third order Runge-Kutta schemes computes with two interims stages the solution of the differential equation, Table 3.2) while Fehlbergs construction of a second

κ	λ	0	1	2	γ_κ
	α_κ	$\beta_{\kappa\lambda}$			
0	0	0			$\frac{1}{4}$
1	$\frac{1}{3}$	$\frac{1}{3}$			0
2	$\frac{2}{3}$	0	$\frac{2}{3}$		$\frac{3}{4}$

Table 3.2: Coefficients of classical third order RK integration scheme with two interims stages

order schemes already consist of two stages as the classic third order scheme. The increased number of evaluations improves the accuracy and will also effect the rate of convergence as observed for different examples in chapter 4.

In the following we briefly discuss the interplay of a second order RK scheme proposed in [10], with the full PIC cycle, as depicted in Figure 3.3. To do this, it is assumed that the electromagnetic fields are given at time $t = t^n$ either by the initial step or the previous iteration as well as the phase space coordinates of the particles with their location in the grid based domain. In the first step in module ① the fields of $E^n; B^n$ are interpolated onto the position of the particles. The first intermediate stage of velocity v^1 and position x^1 of the particles is calculated by the Lorentz solver in module ②. With module ③ the particle based charge and current density at time t^n is assigned to grid points needed to compute the electromagnetic fields at intermediate time level t^1 by the field solver in module ④. The first intermediate stage is now complete and this

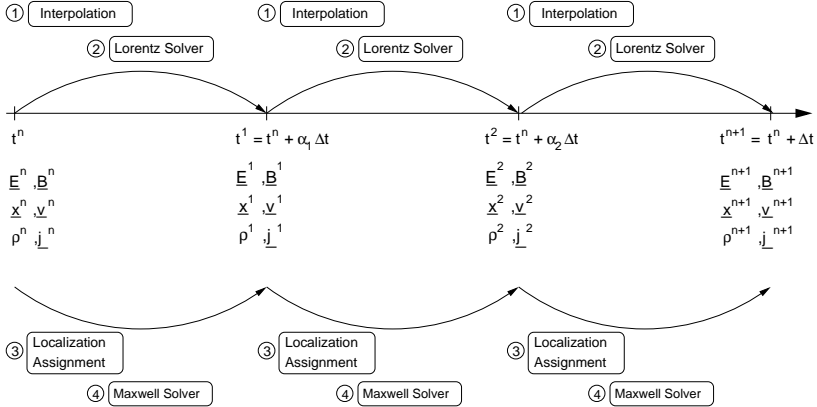


Figure 3.3: Second order Runge-Kutta integration method proposed by Fehlberg with two interim stages for the purpose of step size control.

procedure starts again to reach the stages t^2 and finally the new time level t^{n+1} . The number of needed intermediate stages depends on the selected order and the chosen type of integration (e.g. with or without step size control). Up to order four for the classic RK schemes and the fifth order for the Fehlbergs family of RK integration the increase of evaluation steps corresponds to the increase of the selected formal order. Beyond this formal order the number of required intermediate stages increases more rapidly than the convergence rate which is known as the Butcher [6] barrier. We point out clearly that the necessity to

run through the complete PIC cycle for each intermediate stage even the most expensive particle parts of the cycle causes a tremendous increase of effort of the RK method with a convergence rate higher than two.

3.3 Taylor Series Expansion

An alternative particle push method with a higher convergence rate than two is the new truncated Taylor series expansion TE approach. The most interesting advantage results from the one step construction, whereby costs of several runs through the PIC cycle as for the RK intermediate stages is saved. The mandatory requirements for the TE based schemes are the higher derivatives in space and time of the electromagnetic fields at time t^n . However with the development of high order method for the numerical solution of the Maxwell equations [25, 27] all needed derivatives are computed naturally by these schemes. In Figure 3.4 the algorithm is schematically depicted. Compared to RK method, the TE scheme is very similar to a calculation of one RK intermediate stage.

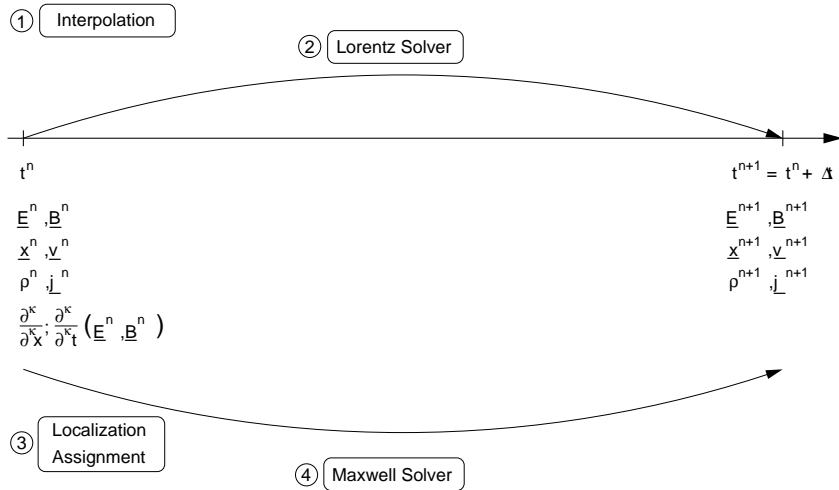


Figure 3.4: Single step Taylor series expansion within the PIC cycle calculates the new phase space components with higher temporal and spatial derivatives of the electromagnetic fields.

The initial situation for this algorithm is the same as for the previously described RK methods, providing the existence of grid-based electromagnetic fields at time t^n and the localized position of the particle within the grid and its phase space coordinates. The algorithm starts at first with module ① to interpolate the electro-

magnetic fields and their derivatives onto the position of the particle. Afterwards, with these informations the Lorentz equations can be integrated numerically by a high order TE scheme implemented now in module ② to obtain particles new velocity and position at time level t^{n+1} . In module ③ particles are localized in the grid domain for the assignment of charge and current density at time level t^n to the mesh which are used as sources for the high order computation of the evolution of the electromagnetic fields up to time level t^{n+1} in module ④.

To describe the mode of operation of the TE technique we once again revisit the characteristics of the Vlasov equation, but now in the convenient form

$$\dot{\underline{U}} = \frac{d\underline{U}}{dt} = \underline{\mathcal{E}}(\underline{x}, t) + \hat{\gamma} \underline{U}(t) \times \underline{\mathcal{B}}(\underline{x}, t), \quad (3.23)$$

$$\dot{\underline{x}} = \frac{d\underline{x}}{dt} = \hat{\gamma} \underline{U}(t) \quad (3.24)$$

where the charge to mass ratio q/m is absorbed in the electromagnetic fields, i.e. $\underline{\mathcal{E}} = \frac{q}{m} \underline{E}(\underline{x}, t)$ and $\underline{\mathcal{B}} = \frac{q}{m} \underline{B}(\underline{x}, t)$. Furthermore, the velocity \underline{v} of the charged particle is replaced by the space component of the 4-velocity \underline{U} [17] (called relativistic velocity in the following) according to

$$\underline{v} = \hat{\gamma} \underline{U}, \quad \hat{\gamma}(\underline{U}) = \left(1 + \frac{\underline{U} \cdot \underline{U}}{c^2} \right)^{-1/2}, \quad (3.25)$$

where $\hat{\gamma}$ denotes the inverse relativistic Lorentz factor and c is the speed of light. Note from (3.23), that the ‘‘acceleration’’ of the charge depends on position and time as well as the relativistic velocity: $\dot{\underline{U}} = \dot{\underline{U}}(\underline{U}, \underline{x}, t)$. Observe further from this relation that

$$\underline{U} \cdot \dot{\underline{U}} = \underline{U} \cdot \underline{\mathcal{E}} \quad (3.26)$$

holds, because the scalar product of \underline{U} with $\underline{U} \times \underline{\mathcal{B}}$ vanishes. In the subsequent analysis we will consider \underline{U} , \underline{x} and t as independent variables. For this it is advantageous to replace the total time derivative of a quantity $\Psi = \Psi(\underline{U}, \underline{x}, t)$ – a scalar or the components of a vector function – by

$$\frac{d\Psi}{dt} = \mathfrak{D}(\Psi) = \mathfrak{D}_c(\Psi) + \mathfrak{D}_U(\Psi), \quad (3.27)$$

where the convective derivative

$$\mathfrak{D}_c = \frac{\partial}{\partial t} + \underline{v} \cdot \nabla_x = \frac{\partial}{\partial t} + \hat{\gamma} \underline{U} \cdot \nabla_x \quad (3.28)$$

acts on space and time dependent quantities while

$$\mathfrak{D}_U = \underline{\dot{U}} \cdot \nabla_U = \sum_{j=1}^3 \dot{U}_j \frac{\partial}{\partial U_j} \quad (3.29)$$

acts only on relativistic velocity dependent expressions. Furthermore, we assume smooth particle trajectories without discontinuous changes in the phase space coordinates like reflection on walls or particle collisions, which will be treated separately in modules for boundary conditions, collisions or chemistry. As well, we suppose that the electromagnetic fields are continuous along the particle trajectory. To obtain a numerical approximation of the phase space coordinates $(\underline{v}, \underline{x})$ with the same order of accuracy as the electromagnetic field solution given from the Maxwell solver, we perform a truncated Taylor series expansion in time up to order P of the particle velocity according to

$$\underline{v}(t) = \sum_{\kappa=0}^P \frac{(t-t_0)^\kappa}{\kappa!} \left[\mathfrak{D}^{(\kappa)}(\hat{\gamma} \underline{U}) \right]_{t_0}, \quad (3.30)$$

where (3.25) is used and

$$\mathfrak{D}^{(\kappa)}(\hat{\gamma} \underline{U}) = \left\{ \mathfrak{D}_c + \mathfrak{D}_U \right\}^{(\kappa)}(\hat{\gamma} \underline{U}). \quad (3.31)$$

Note that the first expansion coefficient $\left[\mathfrak{D}^{(0)}(\hat{\gamma} \underline{U}) \right]_{t_0}$ is nothing else than $\underline{v}_0 = \underline{v}(t_0)$. A straightforward integration over the time interval $[t_0, t]$ yields the charged particle position

$$\begin{aligned} \underline{x}(t) &= \underline{x}_0 + \int_{t_0}^t \underline{v}(s) ds \\ &= \underline{x}_0 + \sum_{\kappa=0}^P \frac{(\Delta t)^{\kappa+1}}{(\kappa+1)!} \left[\mathfrak{D}^{(\kappa)}(\hat{\gamma} \underline{U}) \right]_{t_0}, \end{aligned} \quad (3.32)$$

where $\underline{x}_0 = \underline{x}(t_0)$ is the initial position and $\Delta t = t - t_0$. It is obvious from the expressions (3.30) and (3.32) that the series expansion up to order P results in a local truncation error of $\mathcal{O}(\Delta t^{(P+1)})$ and $\mathcal{O}(\Delta t^{(P+2)})$ for the velocity and position, respectively.

What remains now to do is to compute simply the κ^{th} derivative of $\hat{\gamma} \underline{U}$ by applying operator (3.27) at $t = t_0$. This is, in principle, a straightforward exercise but

implies cumbersome and lengthy calculations because the operator $\mathfrak{D}(\cdot)$ itself depends on (relativistic) velocity, space and time. In the remaining part of this chapter we develop a strategy which allows a recursive computation of high order derivatives of the particle velocity. All high order derivatives of a product of two functions – at $t = t_0$ – are computed in a common manner by the Leibniz rule as

$$\mathfrak{D}^{(\kappa)}(\hat{\gamma} \underline{U}) = \sum_{\nu=0}^{\kappa} \binom{\kappa}{\nu} \mathfrak{D}^{(\nu)}(\hat{\gamma}) \mathfrak{D}^{(\kappa-\nu)}(\underline{U}), \quad (3.33)$$

where $\binom{\kappa}{\nu} = \frac{\kappa!}{\nu! (\kappa-\nu)!}$. Clearly, for an evaluation of (3.33) all higher derivatives of the inverse Lorentz factor and the relativistic velocity are needed, which are calculated separately in recursive manner. The first conclusion which can be drawn from equation (3.33) is, that if all derivatives on the rhs of (3.33) are known up to order $k < \kappa$, the next order $k + 1 \leq \kappa$ requires only the computation of two additional derivatives, namely, $\mathfrak{D}^{(k+1)}(\hat{\gamma})$ and $\mathfrak{D}^{(k+1)}(\underline{U})$. This is shown in the following for the first three derivatives of $\hat{\gamma} \underline{U}$:

$$\begin{aligned} \mathfrak{D}^{(0)}(\hat{\gamma} \underline{U}) &= \hat{\gamma} \underline{U} \\ \mathfrak{D}^{(1)}(\hat{\gamma} \underline{U}) &= \mathfrak{D}^{(1)}(\hat{\gamma}) \underline{U} + \hat{\gamma} \mathfrak{D}^{(1)}(\underline{U}) \\ \mathfrak{D}^{(2)}(\hat{\gamma} \underline{U}) &= \mathfrak{D}^{(2)}(\hat{\gamma}) \underline{U} + 2 \mathfrak{D}^{(1)}(\hat{\gamma}) \mathfrak{D}^{(1)}(\underline{U}) + \hat{\gamma} \mathfrak{D}^{(2)}(\underline{U}) \\ \mathfrak{D}^{(3)}(\hat{\gamma} \underline{U}) &= \mathfrak{D}^{(3)}(\hat{\gamma}) \underline{U} + 3 \mathfrak{D}^{(2)}(\hat{\gamma}) \mathfrak{D}^{(1)}(\underline{U}) + 3 \mathfrak{D}^{(1)}(\hat{\gamma}) \mathfrak{D}^{(2)}(\underline{U}) + \hat{\gamma} \mathfrak{D}^{(3)}(\underline{U}). \end{aligned}$$

Now, we first follow the path of high order derivative computations of the inverse Lorentz factor and afterwards present that one for the relativistic velocity.

3.3.1 High Order Derivatives of the Inverse Lorentz Factor

Since the inverse Lorentz factor (3.25) depends only on the relativistic velocity, we immediately obtain for the first application of operator (3.27) to $\hat{\gamma}$ the result

$$\mathfrak{D}^{(1)}(\hat{\gamma}) = \mathfrak{D}_U(\hat{\gamma}) = -\frac{\hat{\gamma}^3}{c^2} \underline{U} \cdot \underline{\mathcal{E}}, \quad (3.34)$$

where relation (3.26) has already been used. Note, that all quantities on the rhs of the latter expression are given at the initial time. Higher order derivatives, i.e.

$2 \leq \nu \leq \kappa$, can easily be determined recursively according to

$$\mathfrak{D}^{(\nu)}(\hat{\gamma}) = \mathfrak{D}^{(\nu-1)}\left(\mathfrak{D}^{(1)}(\hat{\gamma})\right) \quad (3.35)$$

$$\begin{aligned} &= -\frac{1}{c^2}\mathfrak{D}^{(\nu-1)}\left(\hat{\gamma}^3 \underline{U} \cdot \underline{\mathcal{E}}\right) \\ &= -\frac{1}{c^2}\sum_{\lambda=0}^{\nu-1}\binom{\nu-1}{\lambda}\mathfrak{D}^{(\lambda)}(\hat{\gamma}^3)\mathfrak{D}^{(\nu-1-\lambda)}(\underline{U} \cdot \underline{\mathcal{E}}), \end{aligned} \quad (3.36)$$

where the Leibniz rule has been applied once again. The discussion of the third term on the rhs of (3.36) is postponed to the next section. However, the recursive character of determining the derivatives of $\underline{U} \cdot \underline{\mathcal{E}}$ is obvious at this stage. To treat the second term on the rhs of (3.36) we use relations (3.25) and (3.26) and observe first that

$$\mathfrak{D}^{(1)}(\hat{\gamma}^n) = -\frac{n}{c^2}\hat{\gamma}^{n+2}\underline{U} \cdot \underline{\mathcal{E}}; \quad n = 1, 2, \dots \quad (3.37)$$

holds. Then, we proceed in the usual manner to find

$$\begin{aligned} \mathfrak{D}^{(\lambda)}(\hat{\gamma}^m) &= \mathfrak{D}^{(\lambda-1)}\left(\mathfrak{D}^{(1)}(\hat{\gamma}^m)\right) \\ &= -\frac{m}{c^2}\sum_{\sigma=0}^{\lambda-1}\binom{\lambda-1}{\sigma}\mathfrak{D}^{(\sigma)}(\hat{\gamma}^{m+2})\mathfrak{D}^{(\lambda-1-\sigma)}(\underline{U} \cdot \underline{\mathcal{E}}), \end{aligned} \quad (3.38)$$

where the result (3.37) has been applied. Now we turn to show the structure of determining high order relativistic velocity derivations.

3.3.2 High Order Derivatives of the Relativistic Velocity

Similar as in the previous section, we first consider the case where the operator (3.27) is applied to the relativistic velocity \underline{U} . However, this is equivalent to consider the third term on the rhs of (3.33) at $\nu = \kappa - 1$. A short calculation yields for the derivation

$$\mathfrak{D}^{(1)}(\underline{U}) = \mathfrak{D}_U(\underline{U}) = \dot{\underline{U}}, \quad (3.39)$$

which is equal to the rhs of (3.23) at the initial time t_0 . In the spirit of the recursive procedure, derivatives of \underline{U} in the range $0 \leq \nu \leq \kappa - 2$ are given by

$$\begin{aligned} \mathfrak{D}^{(\kappa-\nu)}(\underline{U}) &= \mathfrak{D}^{(\kappa-\nu-1)}\left(\mathfrak{D}^{(1)}(\underline{U})\right) = \mathfrak{D}^{(\kappa-\nu-1)}(\underline{\mathcal{E}}) + \mathfrak{D}^{(\kappa-\nu-1)}(\hat{\gamma}\underline{U} \times \underline{\mathcal{B}}) \\ &= \mathfrak{D}^{(\kappa-\nu-1)}(\underline{\mathcal{E}}) \\ &+ \sum_{\mu=0}^{\kappa-\nu-1}\binom{\kappa-\nu-1}{\mu}\mathfrak{D}^{(\mu)}(\hat{\gamma}\underline{U}) \times \mathfrak{D}^{(\kappa-\nu-1-\mu)}(\underline{\mathcal{B}}), \end{aligned} \quad (3.40)$$

where the result (3.39) with the acceleration (3.23) is taken into account. In fact, the latter relationship nicely reveals that only low order derivatives of $\hat{\gamma}\underline{U}$ enter in the computation for all ν and, furthermore, high order derivatives of the electromagnetic fields $\underline{\mathcal{F}} \in \{\underline{\mathcal{E}}, \underline{\mathcal{B}}\}$ are now required. The first derivative, i.e. $\nu = \kappa - 2$, of the fields simply reads as

$$\mathfrak{D}^{(1)}(\underline{\mathcal{F}}) = \mathfrak{D}_c(\underline{\mathcal{F}}) = \left\{ \frac{\partial}{\partial t} + \hat{\gamma}\underline{U} \cdot \nabla_x \right\} \underline{\mathcal{F}}, \quad (3.41)$$

because they depend only on position and time. However, this derivation of electromagnetic fields depends now also on the relativistic velocity \underline{U} . To find systematic expressions for high order derivatives of the electromagnetic fields, we notice that the commutator relations

$$\left[\frac{\partial}{\partial t}, \mathfrak{D} \right] (\Psi) = \frac{\partial}{\partial t} \mathfrak{D}(\Psi) - \mathfrak{D} \left(\frac{\partial \Psi}{\partial t} \right) = \frac{\partial \dot{U}_k}{\partial t} \frac{\partial \Psi}{\partial U_k} \quad (3.42)$$

and

$$\left[\frac{\partial}{\partial x_j}, \mathfrak{D} \right] (\Psi) = \frac{\partial}{\partial x_j} \mathfrak{D}(\Psi) - \mathfrak{D} \left(\frac{\partial \Psi}{\partial x_j} \right) = \frac{\partial \dot{U}_k}{\partial x_j} \frac{\partial \Psi}{\partial U_k} \quad (3.43)$$

for $\Psi = \Psi(\underline{U}, \underline{x}, t)$ holds, where the usual summation convention - that is, repeated indices are summed - is applied. Since the fields do not depend on the relativistic velocity, we obtain

$$\left[\frac{\partial}{\partial t}, \mathfrak{D} \right] (\underline{\mathcal{F}}) = \left[\frac{\partial}{\partial x_j}, \mathfrak{D} \right] (\underline{\mathcal{F}}) = 0, \quad (3.44)$$

which means that the order of differentiation can be interchanged. Due to this fact, higher order derivatives of relation (3.41) are given by

$$\begin{aligned} \mathfrak{D}^{(m+1)}(\underline{\mathcal{F}}) &= \frac{\partial}{\partial t} \mathfrak{D}^{(m)}(\underline{\mathcal{F}}) \\ &+ \sum_{i=0}^m \binom{m}{i} \mathfrak{D}^{(i)}(\hat{\gamma}\underline{U}) \cdot \nabla_x \mathfrak{D}^{(m-i)}(\underline{\mathcal{F}}), \end{aligned} \quad (3.45)$$

where $m = 1, 2, \dots$. Clearly, since $\mathfrak{D}^{(i)}(\hat{\gamma}\underline{U})$ and $\mathfrak{D}^{(m-i)}(\underline{\mathcal{F}})$ are already determined in the previous “step”, a recursive sequence of the derivation of the fields by the complicated operator $\mathfrak{D}(\cdot)$ is established by (3.41) and (3.45) while the high order time and space derivatives of $\underline{\mathcal{E}}$ and $\underline{\mathcal{B}}$ are provided by the Maxwell solver.

3.4 General Aspects of Implementation

The accuracy of the proposed high order scheme achieves very fast the computational double precision already with a formal fifth order scheme. The sum of small rounding errors during the algorithm may cause the failure of the expected experimental order of convergence during the tests.

Such a precision problem, for instance, arise in the calculation of the ν -th derivative of the inverse Lorentz factor $\hat{\gamma}$ described by equation (3.36). During the computation, the factor of $1/c^2$ is multiplied $\nu - 1$ times with lower derivative inside the sum and, hence, temporarily the factor of $(1/c^2)^{\nu-1} \approx [1.1 \cdot 10^{-17}]^{\nu-1}$ occurs. The opposite part of this very small term arise from the derivatives of the product $\underline{U} \cdot \underline{\mathcal{E}}$ where the factor of q/m delivered by $\underline{\mathcal{E}}$ is multiplied with the ν derivative of \underline{U} . The derivative is described in equation (3.40) and contains $\nu - 1$ times field derivatives with the factor of charge mass ratio and, hence, in case of an electron temporarily a factor of $(q/m)^{\nu-1} \approx [1.76 \cdot 10^{11}]^{\nu-1}$ occurs. The loss of accuracy is caused by performing the addition of positive and negative terms of the in equation (3.36) without paying specific attention to rounding errors caused by the extreme factors. To take care of the problem a simple modification in the order of calculation is done. In all parts of the sum the factor $(\frac{q}{mc^2})^\nu \approx [1.96 \cdot 10^{-6}]^\nu$ is calculated at first and afterwards the rest of the sum.

A further important aspect is the recursive construction of the derivative operators. This technique offers the possibility to obtain the next higher total derivative of field quantity $\underline{\mathcal{F}}$ only by a rearrangement of previously defined operators applied to given partial derivatives in time and space of the electromagnetic fields components. For example a third order TE scheme as given in Appendix A needs the second total derivative of all field components \mathcal{F}_i and the formulas can be written as

$$\mathfrak{D}^0(\mathcal{F}_i) = \mathcal{F}_i \quad (3.46)$$

$$\mathfrak{D}^1(\mathcal{F}_i) = \frac{\partial}{\partial t} \mathcal{F}_i + \underline{v} \nabla_x \mathcal{F}_i \quad (3.47)$$

$$\mathfrak{D}^2(\mathcal{F}_i) = \mathfrak{D}^1\left(\frac{\partial}{\partial t} \mathcal{F}_i\right) + \mathfrak{D}^1(\underline{v}) \nabla_x \mathcal{F}_i + \underline{v} \mathfrak{D}^1(\nabla_x \mathcal{F}_i). \quad (3.48)$$

The operator to calculate the first total derivative (3.47) uses the folder “Data of Derivatives of Field Component \mathcal{F}_1 ” see Figure 3.5, where all needed partial derivatives are given and stored at the first level of the folder. The first total derivative, consist of a sum of the temporal derivative and the product of the

partial derivatives in space and the velocity.

The second total derivative operator (3.48) consist of three terms. To calculate the first one, the operator \mathfrak{D}^1 uses the folder of the first partial derivative in time called “Data of Derivatives of Field Component $\mathcal{F}_{1,t}$ ” which contains itself the needed partial derivatives in time and space to compute the first total derivatives of $\mathcal{F}_{1,t}$.

The second term can immediately be evaluated because of the given derivative of the velocity by equation (3.33) and the given partial derivatives in space of \mathcal{F}_i .

For the third term in (3.48) the \mathfrak{D}^1 operator is applied to the vector of spatial derivatives of \mathcal{F}_i by performing the calculation for each component separately. For this the \mathfrak{D}^1 operator works on each folder called “Data of Derivatives of Field Component $\mathcal{F}_{1,x}$, $\mathcal{F}_{1,y}$ and $\mathcal{F}_{1,z}$ ” where all needed data of the second partial derivatives of the field components $\mathcal{F}_{1,x}$, $\mathcal{F}_{1,y}$ and $\mathcal{F}_{1,z}$ are stored. Afterwards the scalar product with velocity \underline{v} is computed. The extension to higher operators \mathfrak{D}^3 , \mathfrak{D}^4 and so on, is always realized by defining four new subfolders, where all needed data are stored in the same structure. For example, the operator \mathfrak{D}^3 contains $\mathfrak{D}^2(\frac{\partial}{\partial t}\mathcal{F}_i)$. To calculate the second total derivative, operator \mathfrak{D}^2 needs all second partial derivative of $\mathcal{F}_{1,t}$, stored in four new subfolders “Data of Derivatives of Field Component $\mathcal{F}_{1,tt}$, $\mathcal{F}_{1,tx}$, $\mathcal{F}_{1,ty}$ and $\mathcal{F}_{1,tz}$ ”.

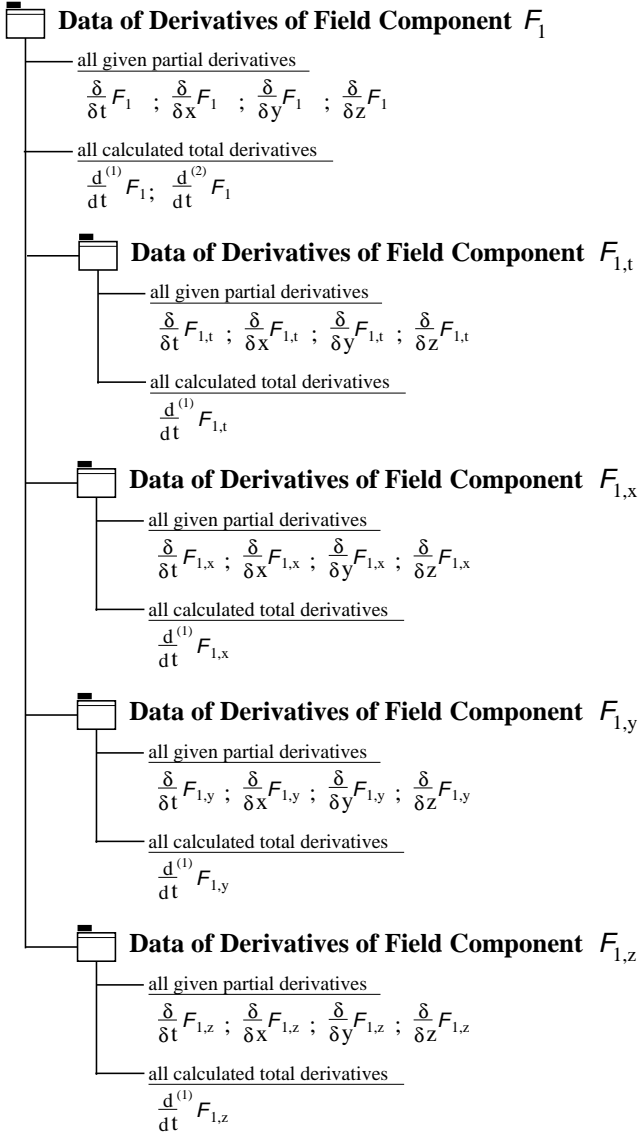


Figure 3.5: Data structure of field component \mathcal{F}_i to sustain the recursive operator construction.

4 Approximation Characteristics and Validation of the Taylor Series Expansion Method

In this section the method of truncated Taylor series expansion is validated and assessed on different examples and compared with results obtained by the two other integration methods introduced in chapter 3. Quantitative statements about the convergence rates are made on examples where an analytic solution is available. For this we compute at the end of the simulation time t_e for a given number of discretization points δ the discrete Euclidian or L_2 -norm of error according to

$$eN(\underline{q}, \delta) = \left\| \underline{q}_{num} - \underline{q}_{ana} \right\|_2^{(\delta)}, \quad (4.1)$$

where \underline{q}_{num} and \underline{q}_{ana} are the numerical and analytical value of quantity \underline{q} at time $t = t_e$. The effective or experimental order of convergence (EOC) for two calculations is determined by

$$EOC = -\log \left(\frac{eN(\underline{q}, \delta_1)}{eN(\underline{q}, \delta_0)} \right) / \log \left(\frac{\delta_1}{\delta_0} \right), \quad (4.2)$$

where δ_0, δ_1 denotes the number of discretization points used for the computation with a coarse and refined time interval.

The initial minimum number of $\delta = 40$ discretization points is successively increased by a factor of 2. With the given number of δ the time step is calculated by $\Delta t = t_e / (\delta - 1)$. To obtain results also for the high order experiments for different refinement levels, which are not affected by machine rounding errors, the computer accuracy is set to quadruple precision for all calculations.

4.1 Non-relativistic Charged Particle Motion

In the first numerical example the properties of the Taylor series expansion scheme is studied for a non relativistic motion, i.e. with a Lorentz factor $\gamma = 1$. For vanishing magnetic induction, Newton's equation of charged particle motion (3.23) with $q = m = 1$ in a spatially constant electric field is given by

$$\underline{\dot{v}}(t) = \underline{\mathcal{E}}(t). \quad (4.3)$$

Each component of the applied oscillating electric field has the form

$$\mathcal{E}_i(t) = \mathcal{E}_0 \sin(\omega_i t + \phi_0); \quad i = 1, 2, 3,$$

where the amplitude \mathcal{E}_0 and the phase shift ϕ_0 in all coordinate directions are fixed and equal to one and $1/2\pi$, respectively, and the frequencies are chosen to be $\omega_1 = 2\pi$, $\omega_2 = 2/3\pi$ and $\omega_3 = 3/2\pi$. Clearly, by construction this problem decouples in the coordinates and the simple equation of motion (4.3) can be immediately integrated. The analytic solution of the phase space coordinates are given by

$$v_i(t) = -\frac{\mathcal{E}_0}{\omega_i} \cos(\omega_i t + \phi_0) + C_{1,i} \quad (4.4)$$

$$x_i(t) = -\frac{\mathcal{E}_0}{\omega_i^2} \sin(\omega_i t + \phi_0) + C_{1,i} t + C_{2,i}, \quad (4.5)$$

where the integration constants are determined from the prescribed initial values $v_i(t_0)$ and $x_i(t_0)$ at time $t_0 = 0$ to be $C_{1,i} = \frac{\mathcal{E}_0}{\omega_i} \cos(\phi_0) + v_i(t_0)$ and $C_{2,i} = \frac{\mathcal{E}_0}{\omega_i^2} \sin(\phi_0) + x_i(t_0)$, respectively. In this example no spatial derivatives of the electric field occur and the total derivative operator reduces to $\mathfrak{D} = \partial/\partial t$. Hence with the TE approach the new velocity (3.30) and location (3.32) of a particle is calculated only with temporal derivatives of the electric field :

$$\underline{v}(t) = \underline{v}_0 + \Delta t \underline{\mathcal{E}}(t_0) + \frac{\Delta t^2}{2} [\partial_t \underline{\mathcal{E}}]_{t_0} + \frac{\Delta t^3}{6} [\partial_t^2 \underline{\mathcal{E}}]_{t_0} + \dots \quad (4.6)$$

$$\underline{x}(t) = \underline{x}_0 + \Delta t \underline{v}_0 + \frac{\Delta t^2}{2} \underline{\mathcal{E}}(t_0) + \frac{\Delta t^3}{6} [\partial_t \underline{\mathcal{E}}]_{t_0} + \frac{\Delta t^4}{24} [\partial_t^2 \underline{\mathcal{E}}]_{t_0} + \dots, \quad (4.7)$$

where ∂_t abbreviates $\partial/\partial t$ and $\Delta t = t - t_0$.

4.1.1 Set up of the Numerical Experiment and Results

In order to perform the numerical experiments we fixed the charge q and mass m of the particle equal to one and choose for the initial condition the values $\underline{x}_0 = (0, 0, 0)^T$ and $\underline{v}_0 = (0, 0, 0)^T$. Furthermore, the final simulation time is set to $t_e = 10 \cdot T_P$, with a period of time $T_P = 2\pi$. To get an insight of the

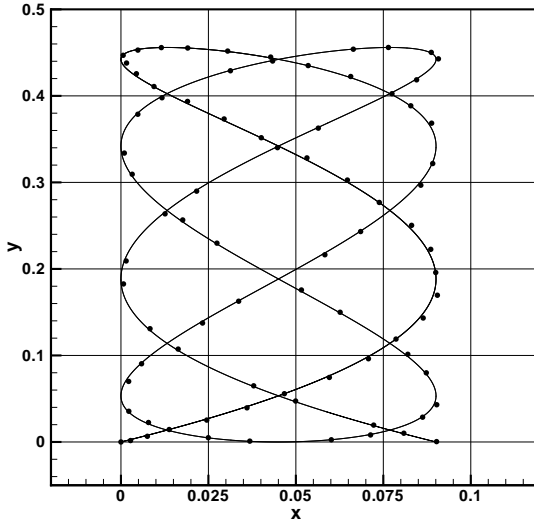


Figure 4.1: The non-relativistic analytic particle motion (line) and the numerical solution (dots) after 10 periods calculated with a formal 5th order TE scheme.

solution characteristics we plot the particle coordinate $y = x_2(t)$ as a function of $z = x_3(t)$ and get the Lissajou figure depicted in Figure 4.1. It is obvious from that plot that the numerical result obtained from a formal 5th order TE scheme (filled circles) is in good agreement with the analytical solution (full line). In order to obtain quantitative information, we calculate the Euclidian norm (4.1) of particle position with the analytic solution (4.5). This norm for position as a function of discretization points δ is plotted in the convergence diagram seen in Figure 4.2. Each of the curves (with numbers) represents the result from a

different formal order TE scheme, $P = 2, \dots, 8$. As a reference Boris LF scheme is plotted as a red line marked with crosses “x”. The slopes of the curves in the double-log scale representation is a measure for the effective convergence rate of the corresponding formal order scheme. For all curves seen in Figure 4.2 the EOC

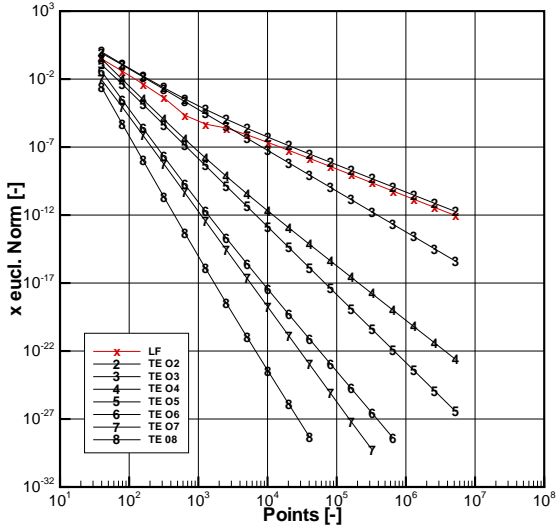


Figure 4.2: The Euclidian error norm of particles position versus the number of discretization points of LF method and different TE schemes.

tends to the selected design (formal) order for all TE as well as for the Boris LF schemes. Furthermore, it is clear from this plot that for a fixed discretization δ the accuracy of the results increases by increasing the formal order of the TE methods. Note, that the increase of accuracy between the formal 4th and 5th order as well as 6th and 7th order schemes is less pronounced. Moreover, the observed decrease of accuracy for discretization points $\delta > 10^5$ of the 8th order TE scheme is due to machine precision.

Roughly the same global convergence behavior is observed from the curves in Figure 4.3, where the Euclidian norm of the particle velocity in dependence of the discretization points δ is shown. A further detailed study of the L_2 error norm and EOC for particles location and velocity is given in the Tables 4.1, 4.2

and 4.3 for the 4th order TE calculation, the second order Boris LF scheme and

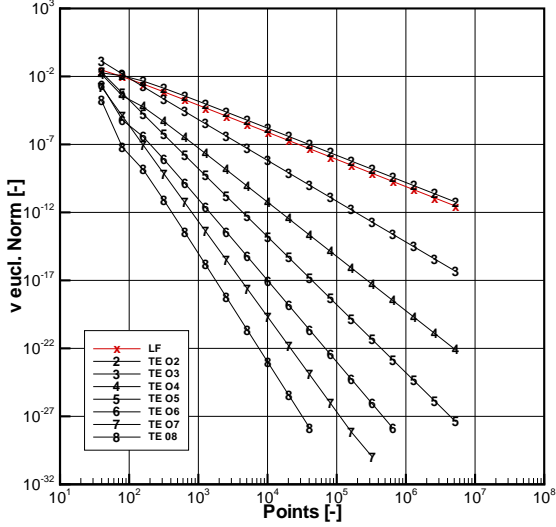


Figure 4.3: The Euclidian error norm of particles velocity versus the number of discretization points of LF method and different TE schemes.

Points	$eN(\underline{v})$	EOC	$eN(\underline{x})$	EOC
1280	1.143e-08		8.893e-09	
2560	6.991e-10	4.06	4.356e-10	4.52
5120	4.321e-11	4.03	2.346e-11	4.35
10240	2.686e-12	4.02	1.349e-12	4.21
20480	1.674e-14	4.01	8.064e-14	4.12

Table 4.1: Euclidian error norm of \underline{x} and \underline{v} in detail and the resulting EOC obtained with a formal 4th order TE scheme for the non-relativistic particle motion.

Points	$eN(\underline{v})$	EOC	$eN(\underline{x})$	EOC
1280	4.743e-5		4.840e-6	
2560	1.195e-5	1.99	2.486e-6	0.96
5120	3.000e-6	1.99	7.809e-7	1.67
10240	7.512e-7	2.00	2.152e-7	1.86
20480	1.880e-7	2.00	5.629e-8	1.93

Table 4.2: Euclidian error norm of \underline{x} and \underline{v} and the resulting EOC obtained from the Boris LF calculation for the non-relativistic particle motion.

the 4th order RK method. It is striking that for all integration methods the euclidian error norm in particle position converge slightly faster than for particles velocity. With a sufficient number of points for the Boris LF scheme the rate of convergence increases up to the second order as for the velocity. By contrast the rate of convergence of the high order RK and TE schemes is evolving down to a final order over the complete range of discretization points (see Tab. 4.1 and 4.3). A comparison between higher order RK (4,5 and 6) and TE (4,5,6,7 and 8)

Points	$eN(\underline{v})$	EOC	$eN(\underline{x})$	EOC
1280	2.242e-11		6.858e-11	
2560	1.522e-12	3.88	3.280e-12	4.56
5120	9.894e-14	3.94	1.735e-13	4.39
10250	6.302e-15	3.97	9.863e-15	4.24
20480	3.976e-16	3.99	5.857e-16	4.14

Table 4.3: The L_2 error norm of \underline{x} and \underline{v} and the resulting EOC computed with a RK method of formal 4th order for non-relativistic particle motion.

schemes is given in Figure 4.4, where the Euclidian error norm of particle location is plotted against the number δ of discretization points. It is conspicuous that the TE scheme of a certain order is always less accurate than the corresponding RK integrators. However, a certain systematic behavior is visible, namely that the accuracy of 4th order RK agrees with 5th order TE scheme. A similar behavior is found for the 6th order RK and 8th order TE approach while the 5th order

RK scheme is nearly bounded by the 6th and 7th order TE integrators. For the

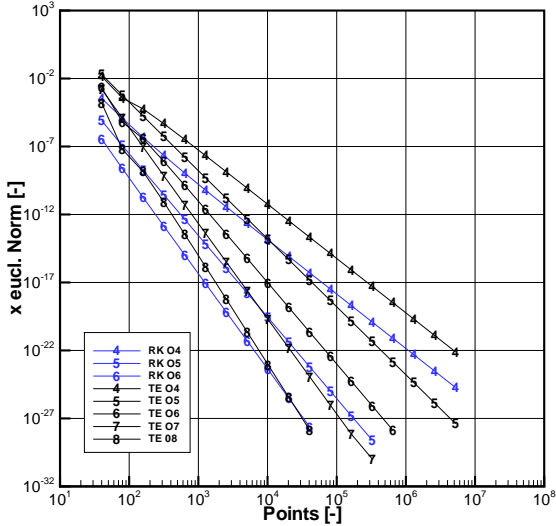


Figure 4.4: Comparison of accuracy between high order RK (4,5 and 6) and TE (4,5,6,7 and 8) schemes.

assessment of the schemes the accuracy is additionally related to the needed *CPU* time for two different cases. In the first "stand alone" case only the module is running to compute particles trajectory separated from all other modules of the PIC cycle. In Figure 4.5 the L_2 error norm of particle position is plotted versus the needed *CPU* time for each computation in the "stand alone" case. In the second case the complete PIC cycle with 1000 particles is used and the needed *CPU* time is plotted in Figure 4.6. As one would expect, the Boris LF scheme is only competitive with the other approaches for a low accuracy range. In general this plot reveals that higher order RK (5 and 6) integrators are more efficient than their TE (5 and 6) counterparts for the present test problem.

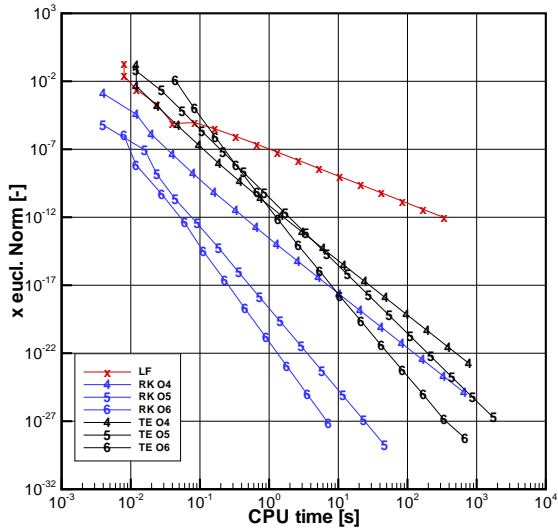


Figure 4.5: Efficiency plot of the LF, RK and TE method in "stand alone" mode.

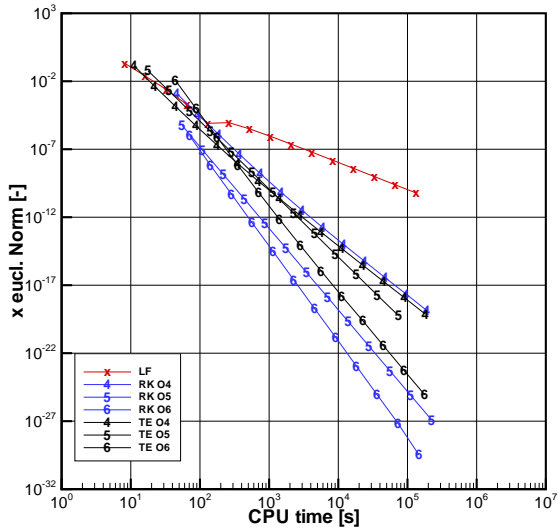


Figure 4.6: Efficiency plot of the LF, RK and TE method test in complete PIC cycle with 1000 particles.

4.2 Particle Motion in a Space and Time Dependent E-Field

For a further assessment of the integration methods introduced in the previous chapter, we consider a one dimensional, non-relativistic test problem where the electric field represents a wave propagating along the x-axis with given frequency ω and wavenumber k (see also [13]). The evolution of phase space coordinates (v, x) of the particle is obtained from

$$\dot{v} = \frac{dv}{dt} = \frac{|q|}{m} E_0 \sin(\omega t - kx) \quad (4.8)$$

$$\dot{x} = \frac{dx}{dt} = v, \quad (4.9)$$

where E_0 denotes the applied constant electrical field, q and m the charge and mass of the particle. In order to get the solution of the nonlinear dynamical system (4.8), (4.9) it is advantageous to use the dimensionless variables

$$\xi = kx - \omega t \quad (4.10)$$

$$\eta = \frac{k}{\omega} v - 1. \quad (4.11)$$

It is immediately obvious from (4.10, 4.11) that $\frac{\partial \xi}{\partial t} = kv - \omega$ and $\frac{\partial \eta}{\partial t} = \frac{k}{\omega} \dot{v}$ hold. With these intermediate results and (4.8) we obtain the autonomous equations

$$-\dot{\eta} = F_1(\xi, \eta) := \frac{\omega_B^2}{\omega} \sin(\xi), \quad (4.12)$$

$$\dot{\xi} = F_2(\xi, \eta) := \omega \eta \quad (4.13)$$

where the bounce frequency $\omega_B^2 = (k|q|E_0)/m$ is introduced. Multiplying both sides of equation (4.12) by ξ and using (4.13), we immediately get

$$\omega \eta \dot{\eta} = -\frac{\omega_B^2}{\omega} \sin(\xi) \dot{\xi}. \quad (4.14)$$

After a further rearrangement, namely dividing by ω and multiplication by dt , the integration of the latter expression yields the result

$$\eta^2(t) = \left[\eta_0^2 - 2Y^2 \cos(\xi_0) \right] + 2Y^2 \cos(\xi), \quad (4.15)$$

where the abbreviation $Y = \omega_B/\omega$ is used (comprises all quantities defining the problem in equation (4.8)) and $\xi_0 = \xi(t_0)$ and $\eta_0 = \eta(t_0)$ denote the initial data of the dimensionless variables (ξ, η) at time $t = t_0$. Note, that the ‘‘forces’’

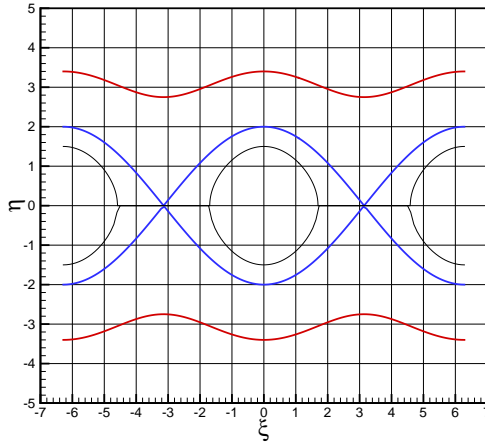


Figure 4.7: Separatrix (blue lines) distinguishes between an open (red lines) and closed (black lines) particle trajectory. The solution for a closed particle trajectory is periodic and exist only for certain values of (ξ, η) pairs.

$F_1 = \partial V / \partial \xi$ and $F_2 = \partial V / \partial \eta$ occurring in the expressions (4.12),(4.13) can be derived from the “potential”

$$V(\xi, \eta) = \frac{\omega}{2} \eta^2 - \frac{\omega_B^2}{\omega} \cos \xi, \quad (4.16)$$

which is a measure of the energy of the particle in the reference frame of wave. Furthermore it can be shown that the area element $\partial \xi \partial \eta$ in phase space does not change in time because $\partial F_2 / \partial \xi = \partial F_1 / \partial \eta = 0$. It is a well known fact [15] that the separatrix (blue line in Fig. 4.7) in the (ξ, η) -plain characterized by

$$\eta_S = \pm Y \sqrt{2[1 + \cos(\xi)]} \quad (4.17)$$

is the limiting curve which distinguishes between open (“rotation type”) and close (“libration type”) trajectory solutions [15]. This means, for instance, that initial data (ξ_0, η_0) chosen outside the separatrix (4.17) leads to open trajectories indicated by the red curves in Figure 4.7. However, for initial values from the interior of the separatrix closed orbit solutions are expected (black curves in Fig. 4.7). Ideally, a particle will trace the closed orbit indefinitely, however, loss of stability

and accuracy of the integration procedure will lead to departures of the exact trajectory. In the following an experimental nonlinear stability analysis and the results of the convergence rate tests are presented.

4.2.1 Set up of the Numerical Experiment and Results

In contrast to the previous example this experiment is suitable to check the TE approach in case of space and time dependent electric field where all convective derivatives are required. This numerical test consist of two parts, the experimental stability analysis and the convergence rate experiment. For both tests, we assume a non-relativistic particle motion, i.e. $\gamma = 1$, where the charge and mass of the particle are set to one. The results presented below are obtained with amplitude E_0 , wavenumber k and an angular velocity ω equal to one. The particle is always initialized at $\xi_0 = 0, \eta_0 = 3/2$ and the exact trajectory is obtained by inserting these values into expression (4.15) and reads as

$$\eta_{\text{ex}} = \pm \frac{1}{2} \sqrt{1 + 8 \cos(\xi)}. \quad (4.18)$$

For the long term stability analysis in the first part a constant final simulation time of $t_e = 800.0$ is used and is equivalent to about 100 orbits of the particle. The effect in stability for different formal orders of the RK and TE schemes compared to the second order Boris LF scheme is considered with a constant timestep of $\Delta t = t_e/(\delta - 1) = 0.8$, which means that the used number of discretization points is $\delta = 1001$.

The second part of this experiment concerns with the evaluation of the convergence rates and for this the final simulation time is selected to $t_e = 80.0$ of about 10 periods. The number of timesteps Δt is successive increased by a factor of two. For the purpose of orientation, the exact trajectory (4.18) with the separatrix (4.17) and the result from the Boris LF integration are plotted in all viewgraphs, where the particle trajectory is analyzed.

First we emphasize that the error of the Boris LF scheme is nearly independent of the number of iterations. Auerbach & Friedman [1] have found out that trapped particle trajectories from the Boris LF integrator exhibit outstanding long-term stability property due to the existence of an invariant which forces the numerical solution to be stable.

The result of the long range third order TE computation is depicted in Figure 4.8. In contrast to the Boris LF integrator (red full line) which keeps the error constant for all times, the particle trajectory computed with the third order TE

scheme is strongly damped to the center of the (ξ, η) -plain. Clearly, this result considerably deviates from the exact solution (black inner curve in Fig. 4.8) and, hence, the **TE** scheme of order three is not applicable in practice. A similar and also not satisfactory behavior is found for the **RK** scheme of order three in the long range limit as it is shown in Figure 4.9. There we see that the third order **RK** result leads to a damped solution where the energy of the particle decreases. Increasing the formal order to four improves clearly the results and reduces the effect of accumulated errors in the calculation with the **TE** scheme. The trajectory in Figure 4.10 is still damped and moves - less pronounced than in Figure 4.8 - towards to the center of the coordinate system. The result for the fourth order **RK** scheme calculation, plotted in Figure 4.11 is only slightly improved. A “fan tracery” behavior to the separatrix is still visible. By using formal orders greater than equal to five deviations from the exact solution (inner trajectory) are no longer obvious for both the **RK** and **TE** method as it is demonstrated by the Figures 4.12 and 4.13. In essence, the second order Boris **LF** scheme shows excellent long term stability properties for simulation times up to $t_e = 800$ compared to the low order **RK** and **TE** methods. However, it has been demonstrated that the lack of stability could be considerably alleviated if multi-stage **RK** and single step **TE** schemes with orders greater than equal to five are used.

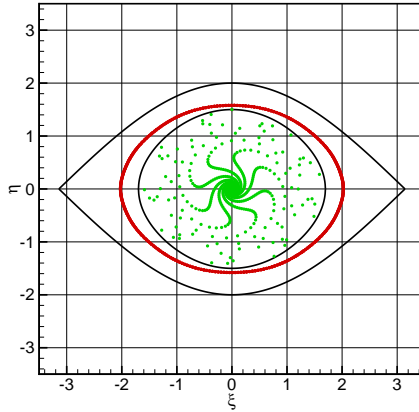


Figure 4.8: Analytic solution (black line) and Boris scheme (red line) compared to the oriental ornament like particle trajectory calculated with third order TE scheme (green dots), which is damped over time to the center of coordinate system.

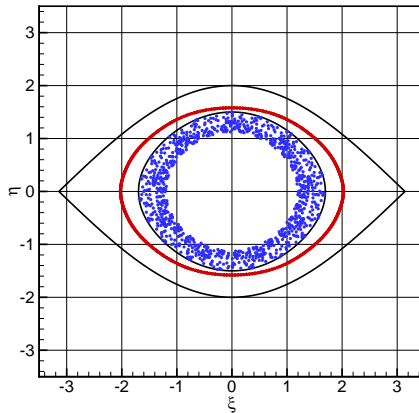


Figure 4.9: The third order RK scheme tends to calculate a damped solution with a set of coefficients proposed by Fehlberg.

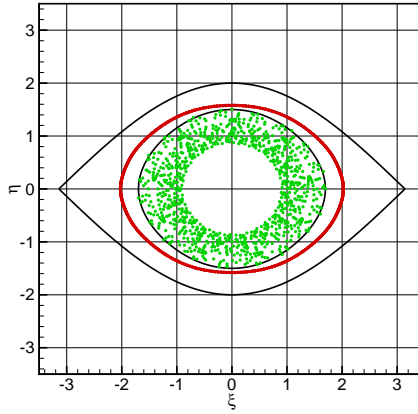


Figure 4.10: Deviation to the analytic solution with a fourth order TE scheme calculation for $t_e = 800$ is reduced but still a visible damped solution occurs.

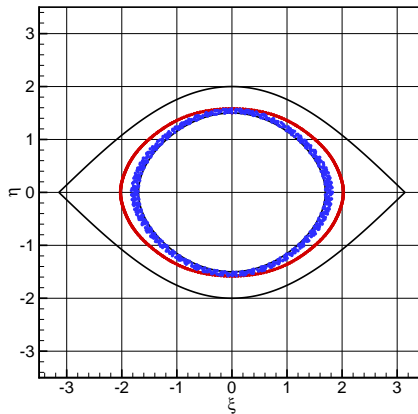


Figure 4.11: The fourth order RK scheme tends to calculate a “fan tracery” solution with a set of coefficients proposed by Fehlberg.

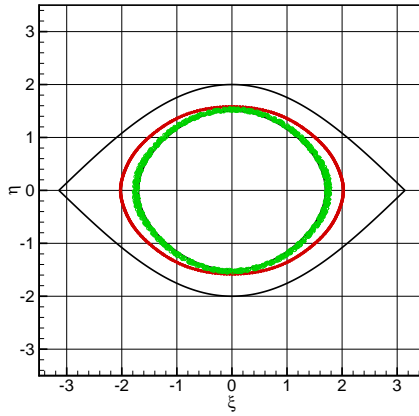


Figure 4.12: Particle trajectory calculated with fifth order TE scheme with no visible errors after $t_E = 800$.

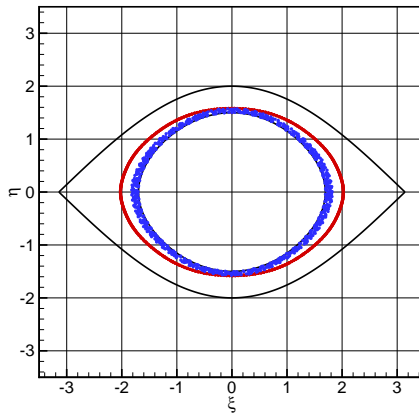


Figure 4.13: The fifth order RK scheme calculation is in accordance with given analytic solution.

In Figure 4.14 the Euclidian error norm (4.1) of the total particle energy - the sum of kinetic and potential energy (see equation (4.16)) - is plotted for the Boris LF integrator (red line) and for the TE schemes from formal order two up to eight as a function of points resolution δ . Clearly, this convergence diagram reveals that

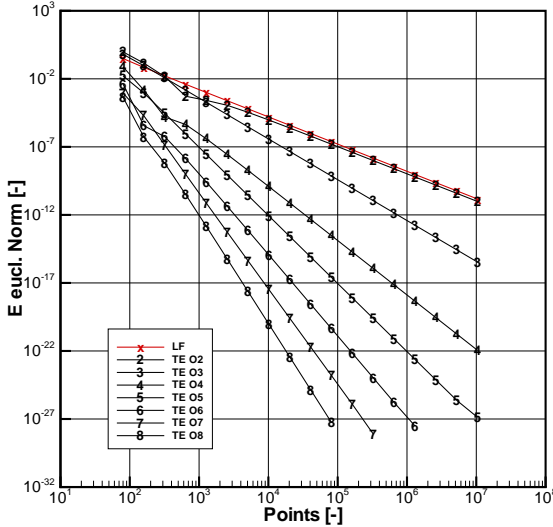


Figure 4.14: The Euclidian error norm of particles energy versus the number of discretization points for the Boris LF scheme and the TE method.

the accuracy of the calculation may be improved either with more discretization points or by an increase of the formal order of the TE scheme. The slopes of all graphs evolve for high numbers of discretization points to a constant value (until machine precision) and the experimental order of convergence (4.2) agrees well with the formal order of the schemes. This is also underscored by Table 4.4, where a detailed convergence study (in the energy norm) for the second order LF and a fifth order RK and TE scheme is listed. Furthermore one reads from plot 4.14 that for the discretization of, for instance, $\delta = 10^4$ points the accuracy spans from $\approx 10^{-5}$ for the second order up to $\approx 10^{-20}$ for the eight order scheme. Vice versa this means, that for a desired accuracy less discretization points and, hence less iterations are

Points	$eN(E)_{LF}$	EOC	$eN(E)_{RK}$	EOC	$eN(E)_{TE}$	EOC
640	3.981e-3		2.070e-07		8.825e-07	
1280	9.816e-4	2.02	6.743e-09	4.94	2.705e-08	5.03
2560	2.445e-4	2.01	2.130e-10	4.98	8.352e-10	5.02
5120	6.106e-5	2.00	6.676e-12	5.00	2.593e-11	5.01
10240	1.526e-5	2.00	2.088e-13	5.00	8.074e-13	5.01

Table 4.4: Convergence rates of energy norm for particle motion in space and time dependent electric field calculated with Boris LF scheme on the left, RK method in the middle and the TE method on right part.

necessary for a high order TE scheme. In Figure 4.15 a comparison between the high order RK and TE (black lines) methods is given. The second order Boris LF scheme (red line) is plotted for orientation. As observed in the first test case in section 4.1, the RK method shows again in parts a higher convergence rate than expected. For instance, the 6th order RK scheme reveals an experimental order of convergence of about seven. This unexpected - more accurate - behavior may be attributed to the special set of coefficients proposed by Fehlberg in [10, 11, 12]. He suggested to use the same number of stages of evaluations but with different coefficients for an error estimation with one order higher than the main integration, as described in section 3.2. Moreover, the convergence rates for the 4th and 5th order RK and TE schemes are roughly comparable, however, the accuracy of RK method is slightly higher than for the TE approach. Finally, in Figure 4.16 the L_2 error norm of the particle energy is plotted versus the CPU time. It is obvious that the LF scheme is only efficient for low accuracy requirements and cannot keep up with the RK and TE methods in the high accuracy range. As already observed previously the high order RK (5th and 6th order) schemes are more efficient for “stand alone” test cases than the TE schemes. For example for an accuracy requirement of 10^{-17} , the 6th order RK need $\approx 1s$ CPU time and the 5th order RK $\approx 10s$ CPU time while the 6th order TE scheme requires $\approx 30s$. However, additional costs, for instance, for particle localization in the PIC cycle in each interim stage of the RK are not included. Note, these cost, accrue only once for the TE schemes. The computational cost for a complete PIC cycle with all particle routines and the field solver is plotted in Figure 4.17. The situation changes between the RK and TE methods due to the multiple run of the complete

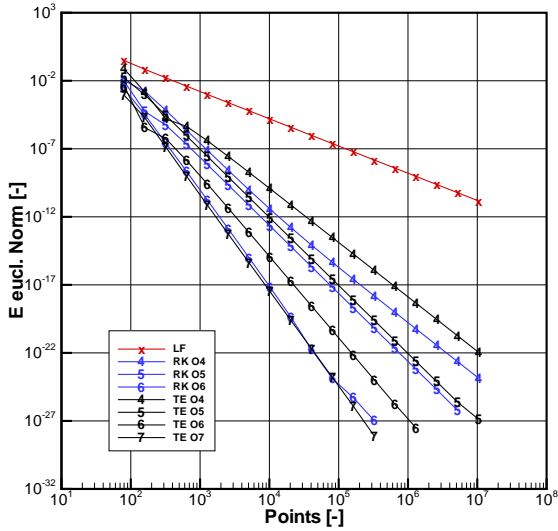


Figure 4.15: EOC rate of Boris LF scheme (red line) compared to RK method (blue lines) of order 4,5,6 and the TE approach (black lines) of order 4 to 7.

PIC cycle for a RK method to calculate the interim stages. The 5th order TE method is about four times faster than the 5th order RK method for all accuracy ranges. For very high accurate results with an error lower than 10^{-25} the 6th order RK becomes about two times faster than the 6th order TE scheme.

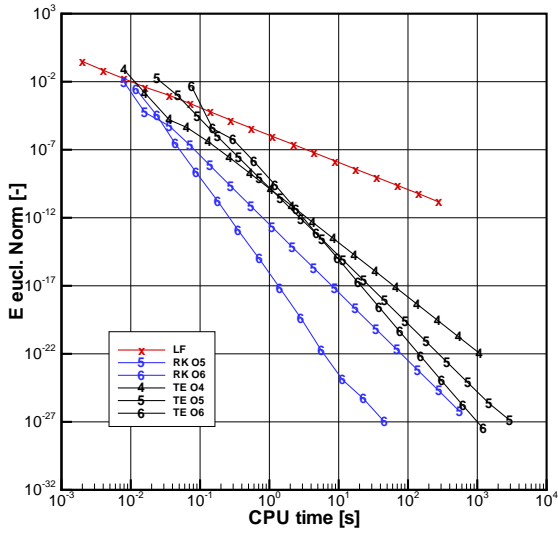
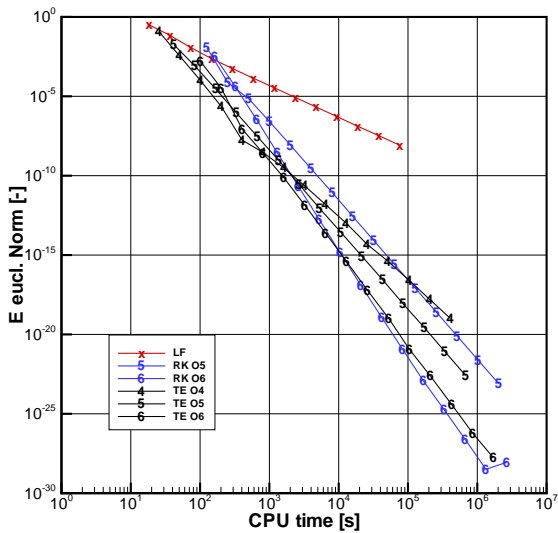


Figure 4.16: Efficiency plot of TE method 4 to 6 compared to Boris LF scheme and RK method 5 and 6.



4.3 Relativistic Particle Motion in a B-Field

The following analytically solvable lable example is chosen to investigate the behavior of the integration schemes under relativistic conditions. The relativistic motion of a positron in a static field of magnetic induction is characterized by an absolute value of velocity and hence, the energy of the particle is conserved. In this case the constant Lorentz factor $\gamma(t_0) = \gamma_0$ is determined by the initial velocity \underline{v}_0 and Newton's equation of motion (3.23) can be simplified to

$$\dot{\underline{v}} = \Omega \underline{v} \times \underline{b} = \Omega \underline{\underline{b}} \underline{v}, \quad (4.19)$$

where $\underline{b} = \frac{\underline{B}}{|\underline{B}|}$, $\Omega = \frac{q|\underline{B}|}{\gamma_0 m}$ and the matrix $\underline{\underline{b}}$ is given by

$$\underline{\underline{b}} = \begin{pmatrix} 0 & b_3 & -b_2 \\ -b_3 & 0 & b_1 \\ b_2 & -b_1 & 0 \end{pmatrix}. \quad (4.20)$$

The ordinary differential equation system can be solved for any given vector of constant magnetic induction \underline{B} and the solution reads as

$$\underline{v}(t) = \begin{pmatrix} b_1^2 + (1 - b_1^2)C & b_1 b_2 (1 - C) + b_3 S & b_1 b_3 (1 - C) - b_2 S \\ b_1 b_2 (1 - C) - b_3 S & b_2^2 + (1 - b_2^2)C & b_2 b_3 (1 - C) + b_1 S \\ b_1 b_3 (1 - C) + b_2 S & b_2 b_3 (1 - C) - b_1 S & b_3^2 + (1 - b_3^2)C \end{pmatrix} \underline{v}_0, \quad (4.21)$$

where $C = \cos(\Omega t)$ and $S = \sin(\Omega t)$ and \underline{v}_0 denotes the initial velocity. To obtain the particle position a further integration of (4.21) can be straightforward performed and yields $\underline{x}(t)$ (see Appendix B.2.1). The resulting trajectory of a charged particle in a constant magnetic induction can always be splitted into a perpendicular and parallel part related to vector \underline{b} . This property is founded by the cross product in (4.19), where only the perpendicular part is leading to a constant circular motion while the parallel part has no effect and constant rectilinear motion parallel to vector \underline{b} occurs. The superposition of both independent parts leads to the classic guiding center motion of a helix like trajectory around a streamline of the magnetic induction with the frequency of gyration of Ω , a periode of time of $T_p = 2\pi/\Omega$ and a Larmor radius of $r_L = |\underline{v}_\perp|/\Omega$. Finally note, that the present test problem is essentially approximated by the TE approach according to

$$\left[\frac{d^\nu}{dt^\nu} \underline{v} \right]_{t_0} = (-1)^\nu \Omega^\nu \underbrace{\underline{b} \times \dots \times \underline{b}}_{\nu\text{-times}} \times \underline{v} \quad ; \quad \nu = 1, 2, \dots \quad (4.22)$$

4.3.1 Set up of the Numerical Experiment and Results

In the present numerical experiment the particle starts from the position $\underline{x}_0^T = (0.0; 0.0; 0.0)m$ with an initial velocity $\underline{v}_0^T = (0.2 \cdot 10^9; 0.0; 0.4 \cdot 10^4)m/s$ which corresponds to a Lorentz factor $\gamma(t) \approx 1.34$. The constant magnetic induction is fixed equal to $\underline{B}^T = (0.0; 0.0; 0.1)V s/m^2$. All computations are performed up to the final simulation time $t_e = 10T_P$ with a period of time $T_P \approx 0.479 \cdot 10^{-9}s$. A first comparison between analytic solution and numerical result which is obtained

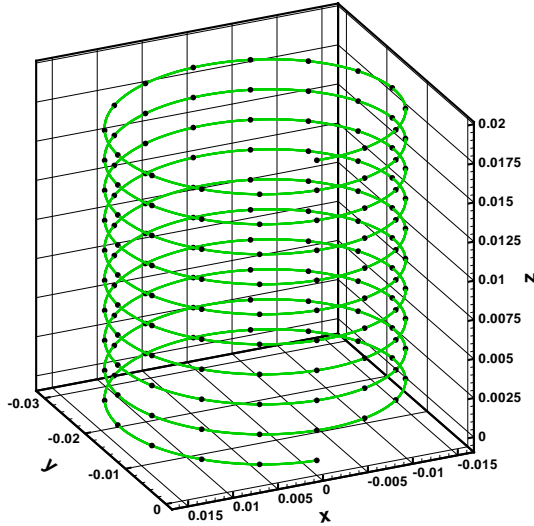


Figure 4.18: The analytic solution (green line) and the numerical result (dots) after 10 periods with 160 discretization points calculated with a formal 6th order TE scheme.

with a formal 6th order TE scheme is depicted in Figure 4.18. Obviously, the analytic helix like trajectory (green line) with a rotation in the xy-plane and a constant movement in z-direction is well resolved by the numerical result (black \bullet). A quantitative insight of the approximation characteristics is given in Figure 4.19, where the Euclidian error norm of particle position is plotted versus the number of discretization points δ for the LF integrator (red line) and for TE schemes

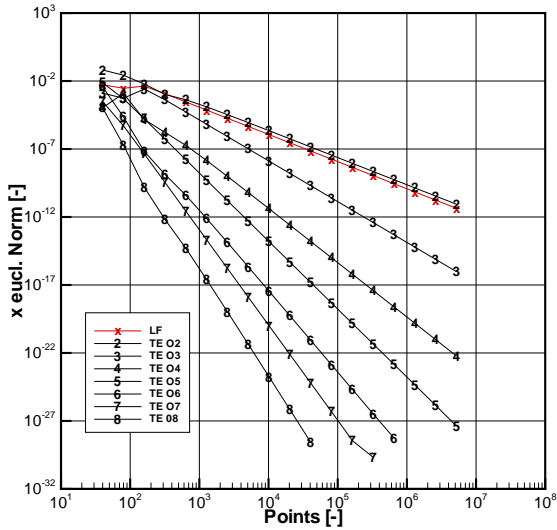


Figure 4.19: The Euclidian error norm versus the number of discretization points for the Boris LF (red line) and different TE schemes up to order eight.

Points	$eN(\underline{v})$	EOC	$eN(\underline{x})$	EOC
40	1.750e+6		1.046e-4	
80	3.260e+3	9.07	1.938e-7	9.08
160	2.700e-0	10.24	1.534e-10	10.30
320	1.004e-2	8.07	6.390e-13	7.91
640	7.933e-5	6.98	4.909e-15	7.02
1280	3.877e-7	7.68	2.385e-17	7.69
2560	1.665e-9	7.86	1.022e-19	7.87
5120	6.798e-12	7.94	4.171e-22	7.94

Table 4.5: Resulting EOC of the Euclidian error norm in \underline{x} and \underline{v} obtained from a formal 8th order TE calculation of particles motion in constant B-field.

from 2nd up to 8th order. From the slopes of the curves we found that in all cases the experimental order of convergence is very close to the formal or design order of the schemes. This is also underlined by the detail study listed in Table 4.5, where the Euclidian error norm of particle position and velocity is used to determine the EOC of a formal 8th order TE scheme. Note that the result of the Boris LF scheme (red line in Fig. 4.19) benefits in this example from the special construction to calculate the cross product in Lorentz force with a slightly more accurate result for all point resolutions compared to the 2nd order TE scheme. The comparison of the approximation behavior between the high order RK and TE

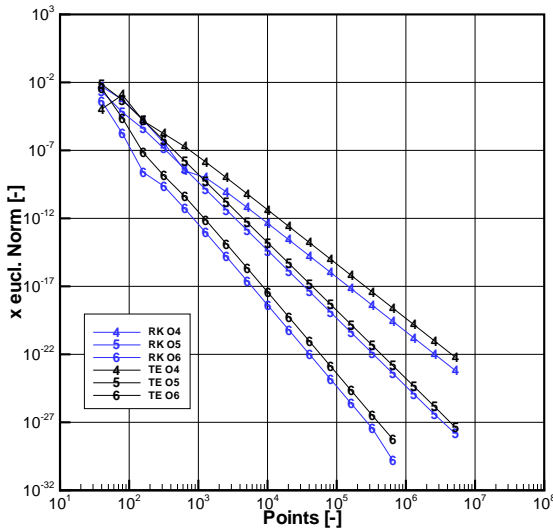


Figure 4.20: Comparable accuracy after 10 periods computed with RK method (blue line) and the TE method (black line) up to order 6.

method is shown in Figure 4.20. Obviously, both high order approaches produce roughly comparable results. A closer look reveals that the RK methods achieve always slightly more accurate results compared to the TE schemes for all selected orders up to six. It is interesting to note that for the present test problem the 6th order RK scheme does not coincide with the 7th order TE scheme as in the previous example. A further numerical result is seen in Figure 4.21, where the L_2

error norm of particles position is plotted against the needed *CPU* time. Clearly,

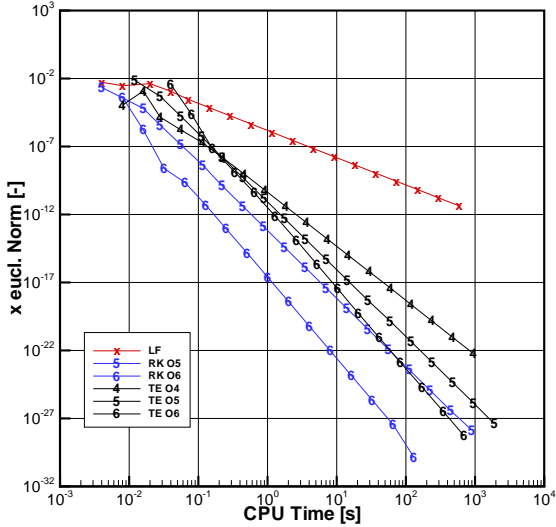


Figure 4.21: Efficiency plot of TE method 4 to 6 compared to Boris LF scheme and RK method 5 and 6. For the stand alone operation mode the most efficient calculation of particles motion in constant B-Field is performed by RK method with a 6th formal order.

the LF scheme cannot compete with the high order methods. Furthermore, we recognize the trend that the 5th and 6th order RK schemes are more efficient than their TE counterparts. However, the efficiency gain, for instance of the 6th order RK compared to the 6th order TE scheme has to be set against the effort of intermediate stage computations for the RK scheme in the environment of PIC simulations. The final test of this example includes the cost of all modules of a PIC cycle. The results are plotted in Figure 4.22 and demonstrate clearly the power of high order methods independent from their different constructions. For example for an accuracy requirement of $eN \approx 10^{-7}$ both high order methods are at least 10 times faster than the LF scheme.

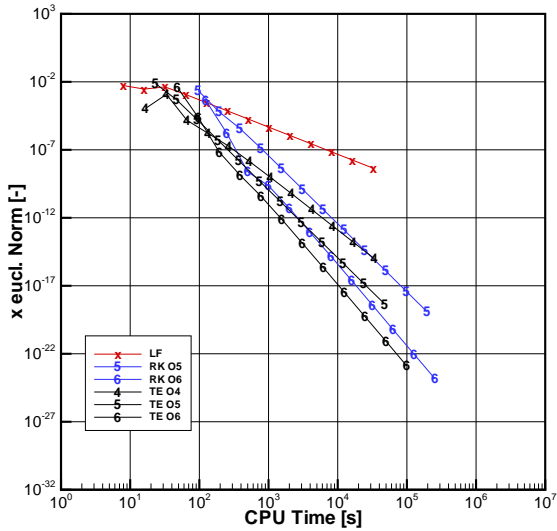


Figure 4.22: Efficiency plot of TE method 4 to 6 compared to Boris LF scheme and RK method 5 and 6. The most efficient calculations in this example where all modules of a PIC cycle are active is performed by TE method with a 6th formal order.

4.4 Relativistic $E \times B$ Drift

The relativistic particle motion in a perpendicularly crossed electric and magnetic field which are constant in time and space can be separated into the cases of $c|\underline{B}| < |\underline{E}|$ and $c|\underline{B}| > |\underline{E}|$ where an analytic solution is described in detail in [17]. The first case leads to a curved and continuously accelerated motion towards the electric field strength. In the present considerations the second case is assumed which is known as the $E \times B$ drift. Particles velocity oscillate up to relativistic region, for that reason this example is suitable to test the nonlinear effect of the relativistic Lorentz factor and, especially to check the operator of calculating the higher derivatives of this factor in the TE scheme. For instance that may be illustrated on the first two derivatives of product $\hat{\gamma}\underline{U}$, see relation (3.33) and Appendix A:

$$\begin{aligned} \mathfrak{D}^{(1)}(\hat{\gamma}\underline{U}) &= \mathfrak{D}^{(1)}(\hat{\gamma})\underline{U} + \hat{\gamma}\underline{\mathcal{E}} + \hat{\gamma}^2 \underline{\mathcal{E}} \times \underline{\mathcal{B}} \\ \mathfrak{D}^{(2)}(\hat{\gamma}\underline{U}) &= \mathfrak{D}^{(2)}(\hat{\gamma})\underline{U} + 2\mathfrak{D}^{(1)}(\hat{\gamma})(\underline{\mathcal{E}} + \hat{\gamma} \times \underline{\mathcal{B}}) + \hat{\gamma}^2 \times \underline{\mathcal{B}} + \hat{\gamma}^3 \times \underline{\mathcal{B}} \times \underline{\mathcal{B}}. \end{aligned}$$

The analytic solution is calculated with the auxiliary coordinate system K' which moves with the drift velocity \underline{v}_D relative to the original system K and is defined as

$$\underline{v}_D = \frac{\underline{E} \times \underline{B}}{B^2}. \quad (4.23)$$

The electromagnetic fields in the frame of reference K' are given by the relation in Appendix B.2. According to these transformations with respect to the drift velocity \underline{v}_D , the electric field vanishes ($\underline{E}' = 0$) in the reference frame K' while the magnetic induction has only a perpendicular component ($\underline{B}'_{\parallel} = 0$ and $\underline{B}'_{\perp} = \underline{B}' = 1/(\gamma\underline{B})$). Then, similar to the previous experiment in section 4.3, we obtain in the coordinate system K' the equation of motion

$$\frac{d\underline{v}'(t')}{dt'} = \Omega' \underline{v}' \times \underline{b}', \quad (4.24)$$

where $\underline{b}' = \frac{\underline{B}'}{|\underline{B}'|}$ and $\Omega' = \frac{q|\underline{B}'|}{\gamma'_0 m}$ with $\gamma'_0 = \gamma'(t'_0)$. The solution in K' is essentially given by expression (4.21) and (B.21). In the original frame of reference system K the solution is immediately given by the inverse transformation from $K' \rightarrow K$ (see eq. (B.11) and (B.11)) by interchanging primed and unprimed quantities and setting $\underline{\beta} \rightarrow -\underline{\beta}$.

4.4.1 Set up of the Numerical Experiment and Results

The simulations for the present example were performed with the same particle constants (m and q) as used in the previous section 4.3. Here, the constant electromagnetic fields are fixed to $\underline{E}^T = (0.0; 0.1 \cdot 10^7; 0.0) V/m$ and $\underline{B}^T = (0.0; 0.0; 0.01) Vs/m^2$. The initial particle position is set to $\underline{x}_0^T = (0.0; 0.0; 0.0) m$ and the velocity was initialized with 99% of the speed of light in y-direction $\underline{v}_0^T = (0.0; 0.99c; 0.0) m/s$, resulting in a Lorentz factor of $\gamma(t_0) \approx 7.1$. The drift velocity for the considered field configuration is given by $\underline{v}_D^T = (0.1 \cdot 10^7; 0.0; 0.0) m/s$ leading to a helical trajectory in xy-plane in the reference frame K with clockwise rotation. This is seen in Figure 4.23, where the analytical solution (green line)

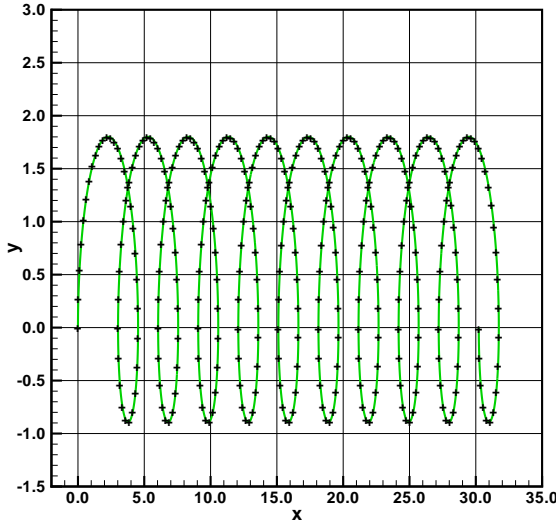


Figure 4.23: Plot of the analytic solution (green line) in reference system K and the numerical results (crosses) after 10 periods with 320 discretization points calculated with a formal 6th order TE scheme.

is compared with the result of a formal 6th order TE scheme (black dots) after 10 periods for 320 discretization points. The convergence behavior obtained for the $\mathbf{E} \times \mathbf{B}$ problem with the TE technique from order two to eight is depicted in

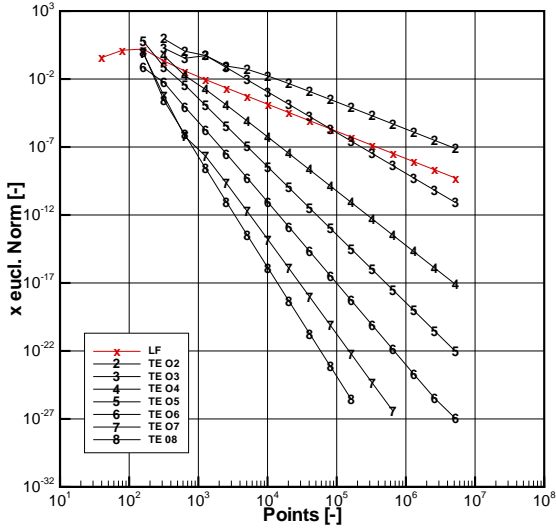


Figure 4.24: Results of the EOC test on $E \times B$ drift example for the Boris LF scheme and different TE schemes up to order eight.

Points	$eN(\vec{v})$	EOC	$eN(\vec{x})$	EOC
1280	4.374e+02		5.613e-07	
2560	7.452e-00	5.88	1.023e-07	5.78
5120	1.215e-01	5.94	1.719e-10	5.89
10240	1.938e-03	5.97	2.784e-12	5.95
20480	3.060e-05	5.99	4.426e-14	5.97

Table 4.6: Euclidian norm of \underline{x} and \underline{v} and resulting EOC obtained from a formal 6th order TE calculation of $E \times B$ example.

Figure 4.24, where the result of the Boris LF scheme (red line) is plotted as a reference. Furthermore the EOC for the 6th order TE scheme for the first five refinement levels is listed in Table 4.25. In both representations (Fig. 4.24 and Tab. 4.25) the final rate of experimental convergence corresponds to the formal design order of the schemes. It is obvious from Figure 4.24, that a design order greater equal than four for the TE method is needed to get a noticeable advan-

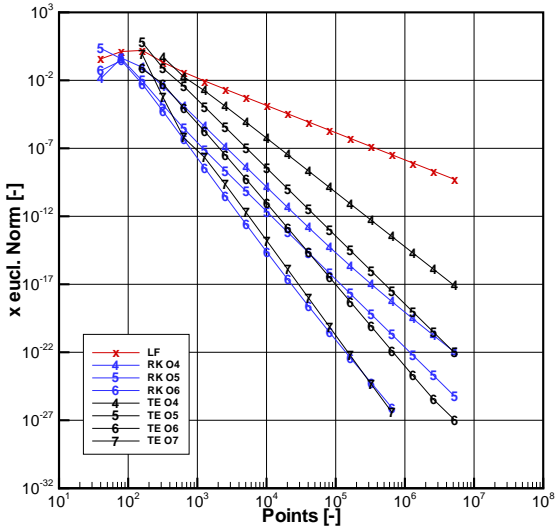


Figure 4.25: Achieved accuracy after 10 periods computed with RK method (blue line) and the Taylor series expansion (black line) up to order 7. The Boris LF scheme result (red line) serve as orientation.

tage in accuracy compared to the Boris LF approach in the coarse discretization region. A comparison between the RK (blue line) and TE (black line) method for the present model problem is given in Figure 4.25, where the results of the LF scheme (red line) serve as orientation. We observe from this plot that lower formal order RK schemes (4,5 and 6) coincide systematically with TE results of formal order 5,6 and 7 respectively. This gap in accuracy is a further hint of the special approximation characteristics of the RK schemes of the Fehlberg family due to the increased number of interims stages for one order higher estimation of

the truncation error. The efficiency of the integrators is compared in Figure 4.26, where the L_2 -norm of error in position is plotted as a function of the needed CPU

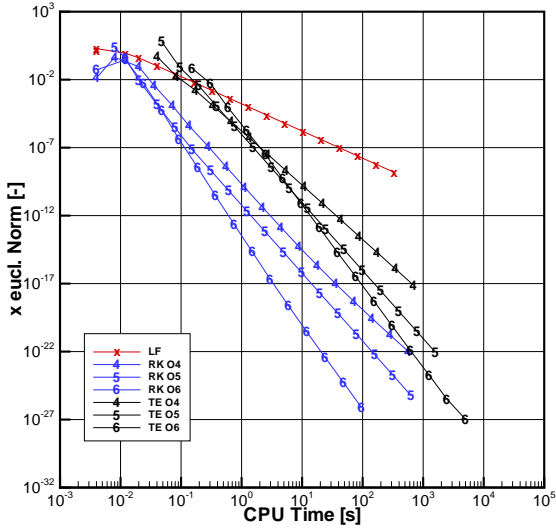


Figure 4.26: Efficiency plot of TE method 4 to 7 compared to Boris LF scheme and RK method 5 and 6.

time for a certain problem size defined by the number of discretization points and formal order. Clearly, for the present "stand alone" problem the RK approach is definitely more efficient than the TE method. In the context of a complete PIC cycle with 1000 particles the advantage of the RK methods is diminish for the benefit of the TE technique see Fig.4.27. In this case the efficiency of 5th order TE scheme is equal to the 5th order RK method.

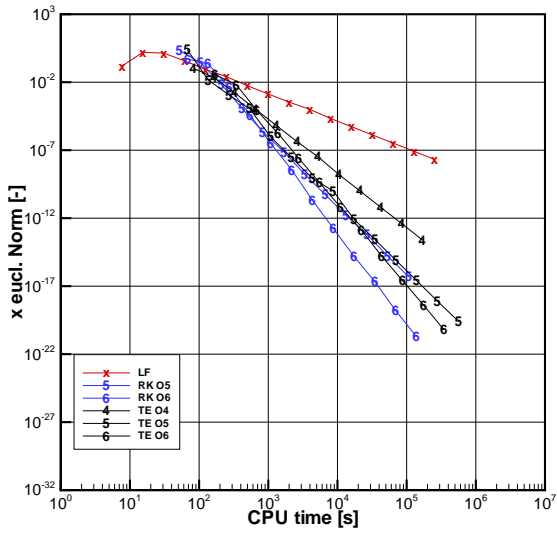


Figure 4.27: Efficiency plot of TE method 4 to 6 compared to Boris LF scheme and RK method 5 and 6.

4.5 Assessment of the Numerical Results

In this section we investigated the approximation behavior of the single-step Taylor expansion schemes from formal *2nd* up to *8th* order. For this purpose we performed numerical experiments for test problems with which different aspects of the numerical approximation of the TE technique could be examined. Furthermore, this new single-step approach for charged particle transport is compared with the classical Boris leapfrog scheme - the “working horse” for the PIC method - and high order (4,5 and 6) Runge-Kutta schemes in the manner of construction proposed by Fehlberg.

The first test problem deals with the non-relativistic motion of a charged particle in time varying electric field only and hence, is appropriate to verify the inclusion of high order temporal derivatives of the electromagnetic fields for the numerical approximation. To get quantitative information from the Lissajou trajectory of the charge as a function of different discretizations of the simulation interval. From the slopes of the curves in the double-log representation we extract the experimental order of convergence and found that this order agrees very well with the formal order (two to eight) of the TE schemes. As it is expected, the second order Boris LF integrator cannot compete in view of accuracy and efficiency with the TE schemes of formal order greater equal than four. The investigation of the RK schemes for the present test case reveals a systematic shift in accuracy compared to the TE integrators, for instance, the accuracy of the *4th* order RK scheme coincides roughly with the *5th* order TE-based scheme. This observation may be a hint to the peculiar construction of the RK schemes of the Fehlberg family. Furthermore, the results show that the RK integrators are more efficient compared to their TE counterparts.

The second test example considers also the non-relativistic motion of a charge but now in a traveling-wave like electric field (which depends on space and time) and is designed to study the approximation behavior when high order convective derivatives are needed in the TE approach. First, we were interested to study the long term stability properties of the Boris integrator as well as the RK- and TE-based schemes experimentally. It is well known that the Boris scheme shows excellent stability properties also for intermediate time step size in the long time limit while the particle trajectory computed with both lower order (three and four) RK and TE integrators indicate less pronounced robustness. Only if the formal order is greater than equal to five, the RK as well as the TE schemes produce

the same satisfactory results which do not visibly deviate from the exact solution. Afterwards, we are concerned with the effective order of convergence of the TE schemes with the design order up to eight, where the Euclidian error norm of total particle energy is used here. For all tested formal orders of the TE approach the measured rate of convergence confirmed the expectation. In general, the comparison of the TE schemes with the Fehlberg RK integration methods shows similar characteristics in EOC and accuracy as already observed for the previous numerical experiment. However it is conspicuous that the curves of the fifth order RK and TE computations for this test problem coincide in the convergence diagram. In view of the efficiency for a complete PIC cycle with 1000 particles we observed, that the TE methods of formal order four and five are more efficient than the RK-based schemes.

The relativistic particle motion in a constant B -field is ideal to asses the approximation characteristics in situations where high order derivatives with respect to the relativistic velocity are necessary for the TE method. In order to get quantitative insight in the approximation properties for this case, we perform the usual convergence study which confirm that all formal orders of the TE schemes are met experimentally. Also the second order Boris LF integrator which is due to its special construction - namely, the decoupling of the electrical and magnetic force contribution and the resulting conservation properties for B -field rotation - also the benchmark for such kind of problems. The comparison between the high order (4,5 and 6) TE and RK schemes reveals that their experimental order of convergence nearly coincide for the present class of problems what was not observed in the previous numerical experiments. Furthermore, we once again found out that the TE schemes of order four to six are more efficient than their multi-stage RK counterparts when the coupling with 1000 particles to the full PIC exist.

The final test problem is concerned with the relativistic motion of a charge in a crossed $E \times B$ configuration for constant electromagnetic fields and tie up to the latter numerical experiment. Here, besides the high order derivatives with respect to the relativistic velocity and, hence the electromagnetic fields, the TE approach requires high order derivatives of the Lorentz factor for the numerical solution of the equations of motion. The quantitative comparison of numerical results with the analytical solution first reveals for all selected formal orders of the TE-based schemes the corresponding rate of convergence. Furthermore, we next observe that the low order (two and three) TE schemes as well as the Boris LF integrator need a certain fineness of the simulation interval in order to deliver acceptable accuracy. However, for formal orders greater than equal to four the accuracy of

the TE integrators is notably higher than that of the Boris scheme. The comparison of the TE schemes with the Fehlberg RK family shows the expected behavior. The TE-based results agree approximately with those of the RK method of one order lower, for instance, the EOC of the 7th order TE scheme coincide with the 6th order RK integration method. Finally, we found from the efficiency diagram the common circumstance, that for the demanding “stand-alone” test problem and the test with the complete PIC cycle with 1000 particles the 6th order RK scheme introduced by Fehlberg is more efficient than those based on the TE approach.

In all previous tests the method of truncated Taylor series expansion applied on the relativistic Newtons equation of motion for charged particles demonstrated for all selected formal orders the corresponding experimental order of convergence. The accuracy and efficiency with a selected formal order of greater than equal four is always higher than for the second order Boris LF scheme. Compared to the RK (5 and 6) methods the accuracy is comparable but the efficiency of the TE scheme is significantly less for all tests of in the “stand-alone” operation mode. The application of the RK scheme in the frame of a complete PIC cycle with 1000 particles induce additional cost caused in repeated execution of the expensive localization of the particle and effect the efficiency in parts for the benefit of the TE method.

5 Conclusion and Outlook

In this work a new high order method for the integration of the relativistic equation of motion for charged particles has been developed and tested successfully on different examples for which analytical solutions are available. This new approach represents the first technique which calculates the new phase space coordinates in a high order single step manner based on a Taylor series expansion TE of particles velocity and position.

The recursive determination of the unknown higher total derivatives of particles velocity is feasible due to the observation that high order derivatives of the relativistic velocity and the inverse Lorentz factor can be computed from the information of the previous derivation order, by the application of simple differentiation rules and from the given high order temporal and spatial as well as mixed derivatives of the electromagnetic fields.

The accuracy of the schemes based on the TE approach depends on the selected truncation order of the Taylor series expansion which is only limited by the provided field derivatives of the Maxwell solver. On different test problems it has been shown that the convergence rate and hence the consistency of the schemes based on this new method agree very well with the selected formal order. Furthermore, a gain in efficiency has been observed by each increase of the selected formal order. Since the TE approach is a type of a single step calculation it saves the costs for multiply passing the whole PIC cycles during one timestep which is necessary for high order Runge-Kutta based algorithms.

The near future goal is to adopt the data structure of the Maxwell-Lorentz solver for the implementation of the TE based schemes. For this it is necessary to develop a high order source term treatment for the numerical solution of the Maxwell equation system. To assess the property of the new high order single step PIC cycle, the interplay of all components have to be investigated under the condition of a simulation where all parts of the program are involved.

With an extension to compute in parallel on several processors an ideal tool for the simulation of non-equilibrium plasma flows is expected. Especially this new high order tool is appropriate to simulate the complex collective plasma dynamics of a PPT. This could help to understand the working principles of such a PPT and to assist the design and optimization process.



Bibliography

- [1] S.P. Auerbach and A. Friedman. Long-time behaviour of numerically computed orbits: Small and intermediate timestep analysis of one-dimensional systems. *J. Comput. Phys.*, 93:189–223, 1991.
- [2] C.K. Birdsall. Particle-in-cell charged-particle simulations, plus Monte Carlo collisions with neutral atoms, PIC-MCC. *IEEE Transaction on Plasma Science*, 19:65–85, 1991.
- [3] C.K. Birdsall and A.B. Langdon. *Plasma Physics via Computer Simulation*. Adam Hilger, Bristol, Philadelphia, New York, 1991.
- [4] J. P. Boris. Relativistic plasma simulations – Optimization of a hybrid code. In *Proc. 4th Conf. on Num. Sim. of Plasmas*, pages 3–67, NRL Washington, Washington DC, 1970.
- [5] J. C. Butcher. Coefficients for the study of Runge-Kutta integration processes. *The Journal of the Australian Mathematical Society*, pages 185–201, 1963.
- [6] J. C. Butcher. On Runge-Kutta processes of high order. *The Journal of the Australian Mathematical Society*, pages 179–194, 1964.
- [7] D. D’Andrea. *Modelling of Intra- and Inter Species Charged Particle Collisions for Flow Simulation in Pulsed Plasma Thrusters*. PhD thesis, Fakultät Luft- und Raumfahrttechnik und Geodäsie, Universität Stuttgart, Germany, 2008.
- [8] D. D’Andrea, C.-D. Munz, and R. Schneider. Modeling of long-range intra- and inter-species charged particle collisions for PIC simulations. *accepted for publications in Communications in Computational Physics*, 7:877–903, 2010.
- [9] M. Fedoruk, C.-D. Munz, P. Omnes, and R. Schneider. A Maxwell-Lorentz solver for self-consistent particle-field simulations on unstructured grids. *Forschungszentrum Karlsruhe – Technik und Umwelt, FZKA 6115*, 1998.

- [10] E. Fehlberg. Classical fifth-, sixth-, seventh-, and eight-order Runge-Kutta formulas with step size control. *NASA TR R-287*, 1968.
- [11] E. Fehlberg. Some experimental results concerning the error propagation in Runge-Kutta type integration formulas. *NASA TR R-352*, 1970.
- [12] E. Fehlberg. Classical eight- and lower-order Runge-Kutta-Nystrom formulas with stepsize control for special second-order differential equations. *NASA TR R-381*, 1972.
- [13] V. Fuchs and J.P. Gunn. On the integration of equations of motion for particle-in-cell codes. *J. Comput. Phys.*, 214:299–315, 2006.
- [14] S. K. Godunov. A difference scheme for numerical solution of discontinuous solution of hydrodynamic equations. *Math.Sbornik, translated US Joint Publ. Res. Service, JPRS 7226*, 47:271–306, 1959.
- [15] H. Goldstein. *Klassische Mechanik*. Akademische Verlagsgesellschaft, Wiesbaden, 1978.
- [16] R. Hockney and J. Eastwood. *Computer Simulation using Particles*. McGraw-Hill, New York, 1981.
- [17] J. D. Jackson. *Classical Electrodynamics*. Wiley, New York, 1999.
- [18] M. Mitchner and C. Kruger. *Partially Ionized Gases*. Wiley, New York, 1973.
- [19] D. Montgomery and D. Tidman. *Plasma Kinetic Theory*. McGraw-Hill, New York, 1964.
- [20] C.-D. Munz, R. Schneider, E. Sonnendrücker, E. Stein, U. Voß, and T. Westermann. A finite-volume particle-in-cell method for the numerical treatment of the Maxwell-Lorentz equations on boundary-fitted meshes. *Int. J. Numer. Meth. Engng.*, 44:461–487, 1999.
- [21] D.R. Nicholson. *Introduction to Plasma Theory*. Wiley, New York, 1983.
- [22] K. Nishikawa and M. Wakatani. *Plasma Physics*. Springer, Berlin, Heidelberg, 2000.
- [23] W. Oevel. *Einführung in die Numerische Mathematik*. Spektrum Akademischer Verlag, Heidelberg, Berlin, Oxford, 1996.

- [24] M. Rosenbluth, W. MacDonald, and D. Judd. Fokker-Planck equation for an inverse-square force. *Phys. Rev.*, 107:1–6, 1957.
- [25] T. Schwartzkopff, F. Lörcher, C.-D. Munz, and R. Schneider. Arbitrary high order finite-volume methods for electromagnetic wave propagation. *Computer Physics Communications*, 174:689–703, 2006.
- [26] I.P. Shkarofsky, T.W. Johnston, and M.P. Bachynski. *The Particle Kinetics of Plasmas*. Addison-Wesley, Reading, 1966.
- [27] A. Taube, M. Dumbser, C.-D. Munz, and R. Schneider. A High Order Discontinuous Galerkin Method with Local Time Stepping for the Maxwell Equations. *International Journal of Numerical Modelling: Electronic Networks, Devices and Fields*, 22(1):77–103, 2009.
- [28] T. Westermann. Numerische Simulation von technisch relevanten Ionen-Dioden mit der Particle-in-Cell Methode. *Kernforschungszentrum Karlsruhe, KfK 4510*, 1989.

Bibliography

A Details on Particle Push Methods

A.1 General Order of Calculation Steps for Taylor Series Expansion

In contrast to a RK scheme a TE scheme increases the rate of convergence only by adding a further derivative terms of $\hat{\gamma}\underline{U}$ to the previously calculated. To evaluate the next term one can reuse interims results of the evaluation steps before. The general order of evaluation of the next higher derivatives of term $\mathfrak{D}^{(\kappa)}(\hat{\gamma}\underline{U})$ depending on κ consist of the following steps.

- 1) field derivative $\mathfrak{D}^{(\kappa-1)}(\underline{\mathcal{E}})$
- 2) term of $\mathfrak{D}^{(\kappa-1)}(\hat{\gamma}^n)$
- 3) $(\kappa - 1)$ -th derivative of product $\underline{U}\underline{\mathcal{E}}$
- 4) κ -th derivative of inverse Lorentz factor $\hat{\gamma}$
- 5) field derivative $\mathfrak{D}^{(\kappa-1)}(\underline{\mathcal{B}})$
- 6) derivative of crossproduct $\mathfrak{D}^{(\kappa-1)}(\underline{U} \times \underline{\mathcal{B}})$
- 7) κ -th derivative of relativistic velocity $\mathfrak{D}^{(\kappa)}(\underline{U})$
- 8) κ -th derivative of Taylor term $\mathfrak{D}^{(\kappa)}(\hat{\gamma}\underline{U})$
- 9) expand Taylor series of particles velocity \underline{v} and position \underline{x}

A.2 TE Method first Order Terms

In the following the order of calculation for all needed terms for a TE scheme with $\mathcal{K} = 1$ is presented. With the given initial values of particles velocity \underline{v} one can immediately evaluate the first terms of the Taylor series expansion formula $\mathfrak{D}^{(0)}(\hat{\gamma}\underline{U}) = \hat{\gamma}\underline{U}$. To calculate the second term $\mathfrak{D}^{(1)}(\hat{\gamma}\underline{U})$ we set $\kappa = 1$.

- 1) $\mathfrak{D}^{(\kappa-1)}(\underline{\mathcal{E}}) = \underline{\mathcal{E}}$
- 2) $\mathfrak{D}^{(\kappa-1)}(\hat{\gamma}^3) = \hat{\gamma}^3$
- 3) $\mathfrak{D}^{(\kappa-1)}(\underline{U}\underline{\mathcal{E}}) = \underline{U}\underline{\mathcal{E}}$
- 4) $\mathfrak{D}^{(\kappa)}(\hat{\gamma}) = -\frac{1}{c^2}\hat{\gamma}^3\underline{U}\underline{\mathcal{E}}$
- 5) $\mathfrak{D}^{(\kappa-1)}(\underline{\mathcal{B}}) = \underline{\mathcal{B}}$
- 6) $\mathfrak{D}^{(\kappa-1)}(\underline{U} \times \underline{\mathcal{B}}) = \underline{U} \times \underline{\mathcal{B}}$
- 7) $\mathfrak{D}^{(\kappa)}(\underline{U}) = \underline{\mathcal{E}} + \hat{\gamma}\underline{U} \times \underline{\mathcal{B}}$
- 8) $\mathfrak{D}^{(\kappa)}(\hat{\gamma}\underline{U}) = \mathfrak{D}^{(1)}(\hat{\gamma})\underline{U} + \hat{\gamma}\mathfrak{D}^{(1)}(\underline{U})$
- 9) $\underline{v} = \hat{\gamma}\underline{U} + \Delta t \mathcal{D}_{t_0}^{(1)}(\hat{\gamma}\underline{U})$
 $\underline{x} = \underline{x}_0 + \Delta t\hat{\gamma}\underline{U} + \frac{\Delta t^2}{2}\mathcal{D}_{t_0}^{(1)}(\hat{\gamma}\underline{U})$

A.3 TE Method second Order Terms

Based on already calculated products and terms one can perform for a TE scheme with $\mathcal{K} = 2; \kappa = 2$ the same order of calculation as presented before.

- 1) $\mathfrak{D}^{(\kappa-1)}(\underline{\mathcal{E}}) = \partial_t^1(\underline{\mathcal{E}}) + \nabla_x \underline{\mathcal{E}} \underline{x}^{(1)}$
- 2) $\mathfrak{D}^{(\kappa-2)}(\hat{\gamma}^5) = \hat{\gamma}^5$
 $\mathfrak{D}^{(\kappa-1)}(\hat{\gamma}^3) = -\frac{3}{c^2} \hat{\gamma}^5 \underline{U} \underline{\mathcal{E}}$
- 3) $\mathfrak{D}^{(\kappa-1)}(\underline{U} \underline{\mathcal{E}}) = \mathfrak{D}^{(1)}(\underline{U}) \underline{\mathcal{E}} + \underline{U} \mathfrak{D}^{(1)}(\underline{\mathcal{E}})$
- 4) $\mathfrak{D}^{(\kappa)}(\hat{\gamma}) = -\frac{1}{c^2} \left(\mathfrak{D}^{(1)}(\hat{\gamma}^3) \underline{U} \underline{\mathcal{E}} + \hat{\gamma}^3 \mathfrak{D}^{(1)}(\underline{U} \underline{\mathcal{E}}) \right)$
- 5) $\mathfrak{D}^{(\kappa-1)}(\underline{\mathcal{B}}) = \partial_t^1(\underline{\mathcal{B}}) + \nabla_x \underline{\mathcal{B}} \underline{x}^{(1)}$
- 6) $\mathfrak{D}^{(\kappa-1)}(\underline{U} \times \underline{\mathcal{B}}) = \mathfrak{D}^{(1)}(\underline{U}) \times \underline{\mathcal{B}} + \underline{U} \times \mathfrak{D}^{(1)}(\underline{\mathcal{B}})$
- 7) $\mathfrak{D}^{(\kappa)}(\underline{U}) = \mathfrak{D}^{(1)}(\underline{\mathcal{E}}) + \mathfrak{D}^{(1)}(\hat{\gamma}) \underline{U} \times \underline{\mathcal{B}} + \hat{\gamma} \mathfrak{D}^{(1)}(\underline{U} \times \underline{\mathcal{B}})$
- 8) $\mathfrak{D}^{(\kappa)}(\hat{\gamma} \underline{U}) = \mathfrak{D}^{(2)}(\hat{\gamma}) \underline{U} + 2\mathfrak{D}^{(1)}(\hat{\gamma}) \mathfrak{D}^{(1)}(\underline{U}) + \hat{\gamma} \mathfrak{D}^{(2)}(\underline{U})$
- 9) $\underline{v} = \hat{\gamma} \underline{U} + \Delta t \mathcal{D}_{t_0}^{(1)}(\hat{\gamma} \underline{U}) + \frac{\Delta t^2}{2} \mathcal{D}_{t_0}^{(2)}(\hat{\gamma} \underline{U})$
 $\underline{x} = \underline{x}_0 + \Delta t \hat{\gamma} \underline{U} + \frac{\Delta t^2}{2} \mathcal{D}_{t_0}^{(1)}(\hat{\gamma} \underline{U}) + \frac{\Delta t^3}{6} \mathcal{D}_{t_0}^{(2)}(\hat{\gamma} \underline{U})$

A.4 TE Method third Order Terms

Steps for a TE method with $\mathcal{K} = 3; \kappa = 3$

- 1)
$$\mathfrak{D}^{(\kappa-1)}(\underline{\mathcal{E}}) = \partial_t^2(\underline{\mathcal{E}}) + \mathfrak{D}^{(0)}(\nabla_x \underline{\mathcal{E}}) \mathfrak{D}^{(1)}(\hat{\gamma} \underline{U}) + \mathfrak{D}^{(1)}(\nabla_x \underline{\mathcal{E}}) \mathfrak{D}^{(0)}(\hat{\gamma} \underline{U})$$
- 2)
$$\begin{aligned} \mathfrak{D}^{(\kappa-3)}(\hat{\gamma}^7) &= \hat{\gamma}^7 \\ \mathfrak{D}^{(\kappa-2)}(\hat{\gamma}^5) &= -\frac{5}{c^2} \hat{\gamma}^7 \underline{U} \underline{\mathcal{E}} \\ \mathfrak{D}^{(\kappa-1)}(\hat{\gamma}^3) &= -\frac{3}{c^2} \left(\mathfrak{D}^{(1)}(\hat{\gamma}^5) \underline{U} \underline{\mathcal{E}} + \hat{\gamma}^5 \mathfrak{D}^{(1)}(\underline{U} \underline{\mathcal{E}}) \right) \end{aligned}$$
- 3)
$$\begin{aligned} \mathfrak{D}^{(\kappa-1)}(\underline{U} \underline{\mathcal{E}}) &= \mathfrak{D}^{(0)}(\underline{U}) \mathfrak{D}^{(2)}(\underline{\mathcal{E}}) \\ &+ 2 \mathfrak{D}^{(1)}(\underline{U}) \mathfrak{D}^{(1)}(\underline{\mathcal{E}}) \\ &+ \mathfrak{D}^{(2)}(\underline{U}) \mathfrak{D}^{(0)}(\underline{\mathcal{E}}) \end{aligned}$$
- 4)
$$\begin{aligned} \mathfrak{D}^{(\kappa)}(\hat{\gamma}) &= -\frac{1}{c^2} \left(\mathfrak{D}^{(0)}(\hat{\gamma}^3) \mathfrak{D}^{(2)}(\underline{U} \underline{\mathcal{E}}) \right. \\ &+ 2 \mathfrak{D}^{(1)}(\hat{\gamma}^3) \mathfrak{D}^{(1)}(\underline{U} \underline{\mathcal{E}}) \\ &+ \left. \mathfrak{D}^{(2)}(\hat{\gamma}^3) \mathfrak{D}^{(0)}(\underline{U} \underline{\mathcal{E}}) \right) \end{aligned}$$
- 5)
$$\mathfrak{D}^{(\kappa-1)}(\underline{\mathcal{B}}) = \partial_t^2(\underline{\mathcal{B}}) + \mathfrak{D}^{(0)}(\nabla_x \underline{\mathcal{B}}) \mathfrak{D}^{(1)}(\hat{\gamma} \underline{U}) + \mathfrak{D}^{(1)}(\nabla_x \underline{\mathcal{B}}) \mathfrak{D}^{(0)}(\hat{\gamma} \underline{U})$$
- 6)
$$\begin{aligned} \mathfrak{D}^{(\kappa-1)}(\underline{U} \times \underline{\mathcal{B}}) &= \mathfrak{D}^{(0)}(\underline{U}) \times \mathfrak{D}^{(2)}(\underline{\mathcal{B}}) \\ &+ 2 \mathfrak{D}^{(1)}(\underline{U}) \times \mathfrak{D}^{(1)}(\underline{\mathcal{B}}) \\ &+ \mathfrak{D}^{(2)}(\underline{U}) \times \mathfrak{D}^{(0)}(\underline{\mathcal{B}}) \end{aligned}$$
- 7)
$$\begin{aligned} \mathfrak{D}^{(\kappa)}(\underline{U}) &= \mathfrak{D}^{(2)}(\underline{\mathcal{E}}) + \mathfrak{D}^{(0)}(\hat{\gamma}) \mathfrak{D}^{(2)}(\underline{U} \times \underline{\mathcal{B}}) \\ &+ 2 \mathfrak{D}^{(1)}(\hat{\gamma}) \mathfrak{D}^{(1)}(\underline{U} \times \underline{\mathcal{B}}) \\ &+ \mathfrak{D}^{(2)}(\hat{\gamma}) \mathfrak{D}^{(0)}(\underline{U} \times \underline{\mathcal{B}}) \end{aligned}$$
- 8)
$$\begin{aligned} \mathfrak{D}^{(\kappa)}(\hat{\gamma} \underline{U}) &= \mathfrak{D}^{(0)}(\hat{\gamma}) \mathfrak{D}^{(3)}(\underline{U}) \\ &+ 3 \mathfrak{D}^{(1)}(\hat{\gamma}) \mathfrak{D}^{(2)}(\underline{U}) \\ &+ 3 \mathfrak{D}^{(2)}(\hat{\gamma}) \mathfrak{D}^{(1)}(\underline{U}) \\ &+ \mathfrak{D}^{(3)}(\hat{\gamma}) \mathfrak{D}^{(0)}(\underline{U}) \end{aligned}$$
- 9)
$$\begin{aligned} \underline{v} &= \hat{\gamma} \underline{U} + \Delta t \mathcal{D}_{t_0}^{(1)}(\hat{\gamma} \underline{U}) + \frac{\Delta t^2}{2} \mathcal{D}_{t_0}^{(2)}(\hat{\gamma} \underline{U}) + \frac{\Delta t^3}{6} \mathcal{D}_{t_0}^{(3)}(\hat{\gamma} \underline{U}) \\ \underline{x} &= \underline{x}_0 + \Delta t \hat{\gamma} \underline{U} + \frac{\Delta t^2}{2} \mathcal{D}_{t_0}^{(1)}(\hat{\gamma} \underline{U}) \\ &+ \frac{\Delta t^3}{6} \mathcal{D}_{t_0}^{(2)}(\hat{\gamma} \underline{U}) \\ &+ \frac{\Delta t^4}{24} \mathcal{D}_{t_0}^{(3)}(\hat{\gamma} \underline{U}) \end{aligned}$$

A.5 Coefficients of Runge-Kutta Integration Schemes

κ	λ	0	1	2	3	γ_κ	$\hat{\gamma}_\kappa$
	α_κ	$\beta_{\kappa\lambda}$					
0	0	0				$\frac{79}{490}$	$\frac{229}{1470}$
1	$\frac{2}{7}$	$\frac{2}{7}$				0	0
2	$\frac{7}{15}$	$\frac{77}{900}$	$\frac{343}{900}$			$\frac{2175}{3626}$	$\frac{1125}{1813}$
3	$\frac{35}{38}$	$\frac{805}{1444}$	$-\frac{77175}{54872}$	$\frac{97125}{54872}$		$\frac{2166}{9065}$	$\frac{13718}{81585}$
4	1	$\frac{79}{490}$	0	$\frac{2175}{3626}$	$\frac{2166}{9065}$		$\frac{1}{18}$

Table A.1: Coefficients for a third order RK integration scheme

κ	λ	0	1	2	3	4	γ_κ	$\hat{\gamma}_\kappa$
	α_κ	$\beta_{\kappa\lambda}$						
0	0	0					$\frac{25}{216}$	$\frac{16}{135}$
1	$\frac{1}{4}$	$\frac{1}{4}$					0	0
2	$\frac{3}{8}$	$\frac{3}{32}$	$\frac{9}{32}$				$\frac{1408}{2565}$	$\frac{6656}{12825}$
3	$\frac{12}{13}$	$\frac{1932}{2197}$	$-\frac{7200}{2197}$	$\frac{7296}{2197}$			$\frac{2197}{4104}$	$\frac{28561}{56430}$
4	1	$\frac{439}{216}$	-8	$\frac{3680}{513}$	$-\frac{845}{4104}$		$-\frac{1}{5}$	$-\frac{9}{50}$
5	$\frac{1}{2}$	$-\frac{8}{27}$	2	$-\frac{3544}{2565}$	$\frac{1859}{4104}$	$-\frac{11}{40}$		$\frac{2}{55}$

Table A.2: Coefficients for a fourth order RK integration scheme

κ	λ	0	1	2	3	4	5	6	γ_κ	$\hat{\gamma}_\kappa$
	α_κ	$\beta_{\kappa\lambda}$								
0	0	0							$\frac{31}{384}$	$\frac{7}{1408}$
1	$\frac{1}{6}$	$\frac{1}{6}$								0
2	$\frac{4}{15}$	$\frac{4}{75}$	$\frac{16}{75}$						$\frac{1125}{2816}$	
3	$\frac{2}{3}$	$\frac{5}{6}$	$-\frac{8}{3}$	$\frac{5}{2}$					$\frac{9}{32}$	
4	$\frac{4}{5}$	$-\frac{8}{5}$	$\frac{144}{25}$	-4	$\frac{16}{25}$				$\frac{125}{768}$	
5	1	$\frac{361}{320}$	$-\frac{18}{5}$	$\frac{407}{128}$	$-\frac{11}{80}$	$\frac{55}{128}$			$\frac{5}{66}$	0
6	0	$-\frac{11}{640}$	0	$\frac{11}{256}$	$-\frac{11}{160}$	$\frac{11}{256}$	0			$\frac{5}{66}$
7	1	$\frac{93}{640}$	$-\frac{18}{5}$	$\frac{803}{256}$	$-\frac{11}{160}$	$\frac{99}{256}$	0	1		$\frac{5}{66}$

Table A.3: Coefficients for a fifth order RK integration scheme

κ	λ	c_{κ}	0	1	2	3	4	5	6	7	8	γ_{κ}	$\hat{\gamma}_{\kappa}$	
			$\beta_{\kappa,\lambda}$											
0	0	0	0									$\frac{77}{1440}$	$\frac{11}{864}$	
1	0	$\frac{2}{33}$	$\frac{2}{33}$									0	0	
2	0	$\frac{4}{33}$	0	$\frac{4}{33}$								0	0	
3	1	$\frac{11}{22}$	1	0	3							$\frac{1771561}{6289920}$	$\frac{32}{105}$	
4	1	$\frac{1}{2}$	$\frac{43}{64}$	0	$-\frac{165}{64}$	77						$\frac{243}{2560}$	$\frac{243}{2560}$	
5	2	$\frac{3}{2}$	$-\frac{2383}{486}$	0	$\frac{1067}{54}$	$-\frac{1701}{1701}$	2176					$\frac{16807}{74880}$	$\frac{16807}{74880}$	
6	6	$\frac{6}{7}$	$\frac{10077}{4802}$	0	$-\frac{5643}{686}$	$\frac{116259}{1701}$	$-\frac{6240}{1701}$	1053				$\frac{11}{270}$	0	
7	1	1	$-\frac{733}{176}$	0	141	16807	216	2401	7203			$\frac{11}{270}$	0	
8	0	0	$\frac{15}{352}$	0	0	$-\frac{5445}{46592}$	18	$-\frac{1215}{5632}$	9152	0		$\frac{11}{270}$	$\frac{11}{270}$	
9	1	1	$-\frac{352}{1833}$	0	144	51237	18	$-\frac{729}{512}$	18304	0	1	$\frac{11}{270}$	$\frac{11}{270}$	

Table A.4: Coefficients for a sixth order RK integration scheme

B Some Results of Special Theory of Relativity

In this appendix we list some basic results from special theory of relativity [17] which are important to comprehend the equations given in the main text (see Section 5.4). For this we consider in the following arbitrary contravariant and covariant 4-vectors (or tensors of rank one) defined by

$$A^\mu = (A^0, \vec{A}) \quad \text{and} \quad A_\mu = (A^0, -\vec{A}) , \quad (\text{B.1})$$

where $A^0 = A_0$ and \vec{A} are the time and space part of the 4-vector, respectively. The scalar product between A^μ and B^μ which is a Lorentz invariant is given by

$$A^\mu B_\mu = A^0 B^0 - \vec{A} \cdot \vec{B} . \quad (\text{B.2})$$

B.1 Transformation of Tensors of Rank one (4-vectors)

Assume that the frame of reference K' is moving with velocity $\vec{u} = c\vec{\beta}_u$ (in arbitrary direction) relative to the inertial reference frame K . An arbitrary 4-vector $W^{\mu'}$ in system K' is obtained from that one $W^\mu = (W^0, \vec{W})$ in frame K according to the transformation

$$W^{0'} = \gamma_u (W^0 - \vec{\beta}_u \cdot \vec{W}) \quad (\text{B.3})$$

$$\vec{W}'_{\parallel} = \gamma_u (\vec{W}_{\parallel} - \vec{\beta}_u W^0) \quad (\text{B.4})$$

$$\vec{W}'_{\perp} = \vec{W}_{\perp} , \quad (\text{B.5})$$

where $\vec{W}'_{\parallel} = \frac{1}{\beta_u^2} (\vec{\beta}_u \cdot \vec{W}) \vec{\beta}_u$, $\vec{W}'_{\perp} = \vec{W} - \vec{W}'_{\parallel}$ and $\gamma_u^{-2} = 1 - |\vec{\beta}_u|^2$. The latter two equations may be combined to one equation which reads as

$$\vec{W}' = \vec{W} + \frac{\gamma_u - 1}{\beta_u^2} (\vec{W} \cdot \vec{\beta}_u) \vec{\beta}_u - \gamma_u W^0 \vec{\beta}_u . \quad (\text{B.6})$$

With the relations (B.3)-(B.5) one can further easily verify that $A^{0'} B^{0'} - \vec{A}' \cdot \vec{B}' = A^0 B^0 - \vec{A} \cdot \vec{B}$ holds. Note, that the inverse transformation $K' \rightarrow K$ is determined from (B.3)-(B.5) by interchanging primed and unprimed quantities and setting $\vec{\beta} \rightarrow -\vec{\beta}$.

B.1.1 Basic 4-vectors

- The time and space 4-vector:

$$x^\mu = (x^0, \vec{x}) \quad (\text{B.7})$$

with $x^0 = ct$.

- The energy-momentum 4-vector:

$$p^\mu = m U^\mu = (p^0, \vec{p}) , \quad (\text{B.8})$$

where $p^0 = m \gamma c$ and $\vec{p} = m \gamma \vec{v}$. The scalar product

$$p_\mu p^\mu = m^2 U_\mu U^\mu = m^2 c^2 \quad (\text{B.9})$$

is an Lorentz invariant.

Other important first-rank tensors are the 4-vector potential and the 4-vector of charge and current density.

B.2 Transformation of electromagnetic Fields

Since the electromagnetic fields are components of the second-rank, antisymmetric field-strength tensor $F^{\mu\nu}$, the transformation from system K to reference frame K' is more difficult. One obtains for the fields in frame K'

$$\vec{E}' = \gamma_u \left[\vec{E} + c \left(\vec{\beta}_u \times \vec{B} \right) \right] - \frac{\gamma_u^2}{\gamma_u + 1} \left(\vec{E} \cdot \vec{\beta}_u \right) \vec{\beta}_u \quad (\text{B.10})$$

$$\vec{B}' = \gamma_u \left[\vec{B} - \frac{1}{c} \left(\vec{\beta}_u \times \vec{E} \right) \right] - \frac{\gamma_u^2}{\gamma_u + 1} \left(\vec{B} \cdot \vec{\beta}_u \right) \vec{\beta}_u , \quad (\text{B.11})$$

where $\vec{\beta}_u = \vec{u}/c$ and $\gamma_u^{-2} = 1 - |\vec{\beta}_u|^2$. The inverse transformation from K' to K is found similar as described above for a 4-vector.

B.2.1 Solution of the Energy-Moment Equation in K'

Since the laws of nature must be covariant, that is invariant in form, under Lorentz transformation we obtain for the energy change and force equations:

- In the reference coordinate system K

$$\frac{dp^0}{dt} = \frac{q}{c} \vec{E} \cdot \vec{v} \Leftrightarrow \frac{d}{dt} (m c^2 \gamma) = q \vec{E} \cdot \vec{v} \quad (\text{B.12})$$

and

$$\frac{d\vec{p}}{dt} = q \left(\vec{E} + \vec{v} \times \vec{B} \right), \quad (\text{B.13})$$

- and in reference frame K'

$$\frac{d}{dt'} (m c^2 \gamma') = q \vec{E}' \cdot \vec{v}' \quad (\text{B.14})$$

$$\frac{d\vec{p}'}{dt'} = q \left(\vec{E}' + \vec{v}' \times \vec{B}' \right) \quad (\text{B.15})$$

where γ' , \vec{v}' and \vec{p}' depend now on t' and \vec{E} and \vec{B} denote the constant external electric field and magnetic induction in K .

In the following we are interested in the situation

$$c^{-1} |\vec{E}| < |\vec{B}|$$

and choose the velocity \vec{u} perpendicular to the orthogonal vectors \vec{E} and \vec{B} ($\vec{E} \cdot \vec{B} = 0$) according to

$$\vec{u} = \frac{1}{|\vec{B}|^2} \vec{E} \times \vec{B}. \quad (\text{B.16})$$

In this case the fields (B.11)-(B.11) in the reference frame K' take the simple form

$$\vec{E}' = \vec{E}_{\parallel}' = \vec{E}_{\perp}' = 0 \quad (\text{B.17})$$

and

$$\vec{B}_{\parallel}' = 0, \quad \vec{B}' = \vec{B}_{\perp}' = \gamma_u^{-1} \vec{B}, \quad (\text{B.18})$$

where \parallel and \perp means parallel and perpendicular to \vec{u} and $\gamma_u^2 = \frac{c^2 |\vec{B}|^2}{c^2 |\vec{B}|^2 - |\vec{E}|^2}$.

Consequently, the equations of motion in K' now reads as

$$\frac{d}{dt'} (m c^2 \gamma') = 0 \Rightarrow \gamma'(t_0') = \gamma_0' \quad (\text{B.19})$$

$$\frac{d\vec{v}'}{dt'} = \Omega' \vec{v}' \times \vec{b}', \quad (\text{B.20})$$

where $\Omega' = \frac{g|\vec{B}'|}{\gamma_0' m}$ and $\vec{b}' = \vec{B}'/|\vec{B}'| = (b_1, b_2, b_3)^T$. The analytical solution of the latter equation is already given in equation (4.21) in section 4.3. With a further integration over time t one obtains the analytic solution of position $\underline{x}'(t')$.

$$\begin{aligned} \underline{x}'(t') = & \\ & \frac{1}{\Omega} \begin{pmatrix} b_1^2 \Omega t + (1 - b_1^2) S & b_1 b_2 (\Omega t - S) - b_3 C & b_1 b_3 (\Omega t - S) + b_2 C \\ b_2 b_1 (\Omega t - S) + b_3 C & b_2^2 \Omega t + (1 - b_2^2) S & b_2 b_3 (\Omega t - S) - b_1 C \\ b_3 b_1 (\Omega t - S) - b_2 C & b_3 b_2 (\Omega t - S) + b_1 C & b_3^2 \Omega t + (1 - b_3^2) S \end{pmatrix} \underline{v}'_0 \\ & + \frac{1}{\Omega} \begin{pmatrix} 0 & b_3 & -b_2 \\ -b_3 & 0 & b_1 \\ b_2 & -b_1 & 0 \end{pmatrix} \underline{v}'_0 + \underline{x}'_0. \end{aligned} \quad (\text{B.21})$$

C Some Properties of the Maxwell Equations

Here, we start from the linear system of conservation laws (2.32) and note first that any linear combination of the matrices $\underline{\underline{K}}_i$ (2.34)

$$\begin{aligned} \underline{\underline{K}} &= \sum_{j=1}^3 n_j \underline{\underline{K}}_j \\ &= \begin{pmatrix} 0 & 0 & 0 & 0 & n_3 c & -n_2 c \\ 0 & 0 & 0 & -n_3 c & 0 & n_1 c \\ 0 & 0 & 0 & n_2 c & -n_1 c & 0 \\ 0 & -n_3 & n_2 & 0 & 0 & 0 \\ n_3 & 0 & -n_1 & 0 & 0 & 0 \\ -n_2 & n_1 & 0 & 0 & 0 & 0 \end{pmatrix} \end{aligned} \quad (\text{C.1})$$

with $\underline{n} \cdot \underline{n} = \sum_{i=j}^3 n_j^2 = 1$, can be diagonalized and all eigenvectors \underline{r}_j , $j = 1, \dots, 6$, are real. Therefore, the Maxwell equations form a linear, hyperbolic system of conservation laws. Furthermore, this system of partial differential equations is called strictly hyperbolic, if it is hyperbolic and the right eigenvectors

$$\begin{aligned} \underline{\underline{R}}_K &= (\underline{r}_1, \dots, \underline{r}_6) \\ &= \begin{pmatrix} c l_1 & c m_1 & c n_1 & 0 & c l_1 & c m_1 \\ c l_2 & c m_2 & c n_2 & 0 & c l_2 & c m_2 \\ c l_3 & c m_3 & c n_3 & 0 & c l_3 & c m_3 \\ -m_1 & l_1 & 0 & n_1 & m_1 & -l_1 \\ -m_2 & l_2 & 0 & n_2 & m_2 & -l_2 \\ -m_3 & l_3 & 0 & n_3 & m_3 & -l_3 \end{pmatrix} \end{aligned} \quad (\text{C.2})$$

of $\underline{\underline{K}}$ form a basis of \mathbb{R}^6 , i.e. these eigenvectors exists and are linear independent. Consequently this means, that

$$\begin{aligned} \underline{\underline{\Lambda}}_K &= \underline{\underline{R}}_K^{-1} \underline{\underline{K}} \underline{\underline{R}}_K = (\lambda_1 \dots, \lambda_6) \\ &= (-c, -c, 0, 0, c, c) \end{aligned} \quad (\text{C.3})$$

holds, where the λ_k 's are the eigenvalues of $\underline{\underline{K}}$ and the inverse matrix of $\underline{\underline{R}}_K$ is given by

$$\underline{\underline{R}}_K^{-1} = \frac{1}{2c} \begin{pmatrix} l_1 & l_2 & l_3 & -cm_1 & -cm_2 & -cm_3 \\ m_1 & m_2 & m_3 & cl_1 & cl_2 & cl_3 \\ 2n_1 & 2n_2 & 2n_3 & 0 & 0 & 0 \\ 0 & 0 & 0 & 2cn_1 & 2cn_2 & 2cn_3 \\ l_1 & l_2 & l_3 & cm_1 & cm_2 & cm_3 \\ m_1 & m_2 & m_3 & -cl_1 & -cl_2 & -cl_3 \end{pmatrix}. \quad (\text{C.4})$$

For the sake of simplicity we introduced in (C.2) and (C.4) two additional unit vectors, namely, $\underline{l} = (l_1, l_2, l_3)^T$ and $\underline{m} = (m_1, m_2, m_3)^T$ with the properties $\underline{n} \cdot \underline{l} = 0$ and $\underline{m} = \underline{n} \times \underline{l}$.

D Exact Riemann solver for Maxwell System of Equations

D.1 General Aspects

In the following we consider the one-dimensional system of conservation laws given by

$$\frac{\partial \underline{u}}{\partial \tau} + \underline{K} \frac{\partial \underline{u}}{\partial \zeta} = 0, \quad (\text{D.1})$$

where $\underline{u} = \underline{u}(\zeta, \tau) \in \mathbb{R}^6$ denotes the vector of state variables (2.33) and $\underline{K} \in \mathbb{R}^{6 \times 6}$ is the constant matrix (C.1). Furthermore, ζ is the space coordinate in direction of the unit vector \underline{n} and τ is the scaled time obtained from $\tau = t - t_0$ with $t_0 \leq t \leq t_1$. Then the RP is defined as an initial value problem for the conservation equation

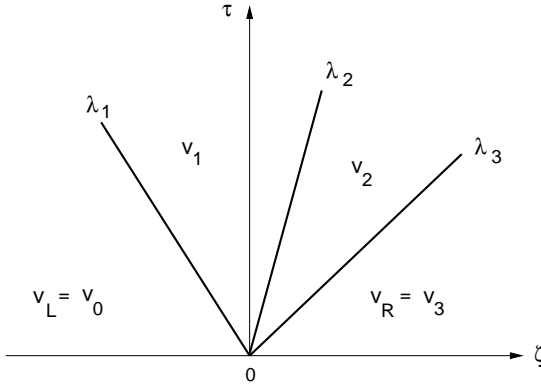


Figure D.1: (ζ, τ) -diagram of the solution of the local RP where $\underline{v} \in \mathbb{R}^3$. Obviously, the solution consists of four constant states $\underline{v}_L, \underline{v}_1, \underline{v}_2$ and \underline{v}_R separated by three characteristics.

(D.1) with piecewise constant initial data of the form

$$\underline{u}(\zeta, 0) = \left\{ \begin{array}{ll} \underline{u}_L & \text{for } \zeta < 0 \\ \underline{u}_R & \text{for } \zeta > 0 \end{array} \right\}, \quad (\text{D.2})$$

which are separated by a single discontinuity at $\zeta = 0$. Here, $\underline{u}_L \in \mathbb{R}^6$ and $\underline{u}_R \in \mathbb{R}^6$ denote the constant left and right state vector with respect to the discontinuity. To obtain the solution of the RP for the strictly hyperbolic Maxwell equations, we take into account that there exists a non-singular matrix \underline{R}_K of right eigenvectors (C.2), so that (C.3) holds. By introducing the characteristic variables

$$\underline{v}(\tau, \zeta) = \underline{R}_K^{-1} \underline{u}(\tau, \zeta) \quad (\text{D.3})$$

and multiplying the conservation system (D.1) from the left with \underline{R}_K^{-1} , we get the decoupled system

$$\frac{\partial \underline{v}}{\partial \tau} + \underline{\Lambda}_K \frac{\partial \underline{v}}{\partial \zeta} = 0, \quad (\text{D.4})$$

of six linear transport equations, where matrix of the eigenvalues $\underline{\Lambda}_K$ is given by (C.3). For the sake of convenience we recast the latter expression into the component form

$$\forall k \in [1, 6]: \quad \frac{\partial v_k}{\partial \tau} + \lambda_k \frac{\partial v_k}{\partial \zeta} = 0 \quad (\text{D.5})$$

and assume for the moment that all eigenvalues λ_k to be non-zero. The solution of the linear advection equations (D.5) is immediately found to be

$$\forall k \in [1, 6]: \quad v_k(\zeta, \tau) = v_k^{(0)}(\zeta - \lambda_k \tau) \quad (\text{D.6})$$

with the initial values obtained from

$$\underline{v}^{(0)}(\zeta) = \underline{R}_K^{-1} \underline{u}(\zeta, 0), \quad (\text{D.7})$$

where $\underline{u}(\zeta, 0)$ is given by the initial data (D.2) (see Fig. D.1). From these relations we conclude, that the characteristic variables at the origin $\zeta = 0$ are given by

$$\forall k \in [1, 6]: \quad \underline{v}(0, \tau) = \underline{v}^{(0)}(-\lambda_k \tau) = \left\{ \begin{array}{ll} v_{R; k} & \text{if } \lambda_k < 0 \\ v_{L; k} & \text{if } \lambda_k > 0 \end{array} \right\}, \quad (\text{D.8})$$

where the constant values $v_{R; k}$ and $v_{L; k}$ are computed from

$$\underline{v}_L = \underline{R}_K^{-1} \underline{u}_L \quad \text{and} \quad \underline{v}_R = \underline{R}_K^{-1} \underline{u}_R, \quad (\text{D.9})$$

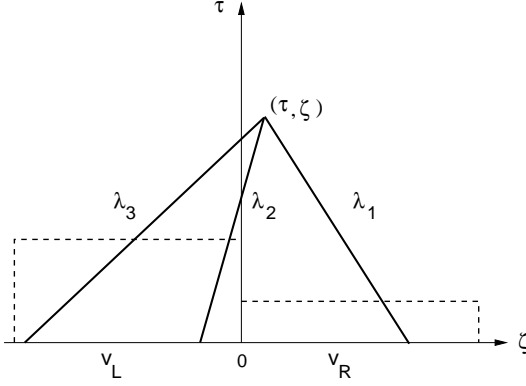


Figure D.2: Different building blocks of a typical PIC simulation program.

respectively. By back transforming of (D.8) according to

$$\underline{u}(0, \tau) = \underline{\underline{R}}_K \underline{v}(0, \tau), \quad (\text{D.10})$$

the solution of the RP (D.1), (D.2) at the origin $\zeta = 0$ is determined. Clearly, the global space-time solution of the RP reads as

$$\underline{u}(\zeta, \tau) = \underline{\underline{R}}_K \underline{v}(\zeta, \tau) = \sum_{k=1}^6 v_k(\zeta, \tau) \underline{\mathcal{L}}_k, \quad (\text{D.11})$$

where $\underline{\mathcal{L}}_k$ is the k th eigenvector of $\underline{\underline{K}}$ with eigenvalue λ_k and the coefficients $v_k(\zeta, \tau)$ are the solution of the linear advection equation.

REMARK: The solution $\underline{u}(0, \tau)$ is a priori not defined if there exists an eigenvalue $\lambda_{k_0} = 0$. However, since the jump of the solution across a characteristic curve is finite, the solution at the characteristic may be explained as an average value of the left and right hand side solution. It can be shown that the definition of the state $\underline{u}(0, \tau)$ in the case where eigenvalues vanish has no influence to the flux calculation.

D.2 Calculation of the Physical Flux

The physical flux function $\underline{F} \in \mathbb{R}^6$ of the strictly hyperbolic Maxwell system at the origin $\zeta = 0$ is given by

$$\underline{F}(\underline{u}(0, \tau)) = \underline{K} \underline{u}(0, \tau) = \underline{R}_K \underline{\Lambda} \underline{v}(0, \tau), \quad (\text{D.12})$$

where relations (D.10) and (C.3) already have been taken into account. Before proceeding we make the observation that the eigenvalues of \underline{K} can be written in the following form

$$\forall k \in [1, 6]: \quad \lambda_k = \lambda_k^+ + \lambda_k^- = \frac{1}{2}(\lambda_k + |\lambda_k|) + \frac{1}{2}(\lambda_k - |\lambda_k|) \quad (\text{D.13})$$

with

$$\lambda_k^+ = \left\{ \begin{array}{l} \lambda_k, \quad \lambda_k > 0 \\ 0, \quad \text{else} \end{array} \right\} \quad \text{and} \quad \lambda_k^- = \left\{ \begin{array}{l} \lambda_k, \quad \lambda_k < 0 \\ 0, \quad \text{else} \end{array} \right\} \quad (\text{D.14})$$

Obviously, this property transfers to the diagonal matrix (C.3) which then reads as

$$\underline{\Lambda} = \underline{\Lambda}^+ + \underline{\Lambda}^- \quad \text{with} \quad \underline{\Lambda}^\pm = \frac{1}{2}(\underline{\Lambda} \pm |\underline{\Lambda}|), \quad (\text{D.15})$$

where $\underline{\Lambda}^+$ and $\underline{\Lambda}^-$ are the diagonal matrices of the positive and negative eigenvalues of \underline{K} , respectively. Inserting the decomposition (D.15) in the last equation of (D.12) and using the relations (D.8) and (D.9), we obtain the intermediate result

$$\underline{R}_K \underline{\Lambda} \underline{v}(0, \tau) = \underline{R}_K \underline{\Lambda}^+ \underline{R}_K^{-1} \underline{u}_L + \underline{R}_K \underline{\Lambda}^- \underline{R}_K^{-1} \underline{u}_R. \quad (\text{D.16})$$

With the definition

$$\underline{K}^\pm = \frac{1}{2}(\underline{K} \pm |\underline{K}|) \quad \text{with} \quad |\underline{K}| = \underline{R}_K |\underline{\Lambda}| \underline{R}_K^{-1}, \quad (\text{D.17})$$

we finally obtain the flux-vector splitting formulation of the total physical flux function at the origin $\zeta = 0$:

$$\underline{F}(\underline{u}(0, \tau)) = \underline{K} \underline{u}(0, \tau) = \underline{K}^+ \underline{u}_L + \underline{K}^- \underline{u}_R. \quad (\text{D.18})$$

This relation reveals that the total flux vector may be regarded as a decomposition into a flux to the “right” – $\underline{K}^+ \underline{u}_L$ – and into a flux to the “left” – $\underline{K}^- \underline{u}_R$ – having respectively only positive and only negative eigenvalues.

Lebenslauf

- 02.05.1975 geboren in Berlin
- Sept. 1981 - Heinrich-Heine Oberschule
Aug. 1990 in Berlin Mitte
- Sept. 1990 - Abitur am Max-Planck Gymnasium
Juni. 1994 in Berlin Mitte
- Okt. 1994 - Grundwehrdienst in der Luftwaffe
Sept. 1995 der Bundeswehr
- Sept. 1995 - Ausbildung zum Fluggerätebauer
Aug. 1998 bei Airbus in Bremen
- Sept. 1998 - Studium der Luft- und Raumfahrttechnik
Juni 2004 an der Universität Stuttgart
- Juli 2004 - Wissenschaftlicher Mitarbeiter am Institut für Aerodynamik
Dez. 2009 und Gasdynamik der Universität Stuttgart
- 2010 Dissertation : *High Order Particle Transport for
PIC Simulations of Plasma Flows*